frontiers | Frontiers in Remote Sensing

ORIGINAL RESEARCH
published: 12 April 2022
doi: 10.3389/frsen.2022.833340

The NASA EPIC/DSCOVR Ocean PAR Product

Robert Frouin[1], Jing Tan[1], Mathieu Compiègne[2], Didier Ramon[2], Marshall Sutton[3], Hiroshi Murakami[4], David Antoine[5,6], Uwe Send[1], Jeff Sevadjian[1] and Vincenzo Vellucci[6]*

[1]Scripps Institution of Oceanography, University of California San Diego, La Jolla, CA, United States, [2]HYGEOS, Euratechnologies, Lille, France, [3]NASA Goddard Space Flight Center, Greenbelt, MD, United States, [4]Earth Observation Research Center, Japan Aerospace Exploration Agency, Ibaraki, Japan, [5]Remote Sensing and Satellite Research Group, School of Earth and Planetary Sciences, Curtin University, Perth, WA, Australia, [6]Laboratoire d'Océanographie de Villefranche, CNRS, Sorbonne Université, Institut de la Mer de Villefranche, Villefranche-sur-Mer, France

The EPIC/DSCOVR observations of the Earth's surface lit by the Sun made from the first Lagrange point several times during the day in spectral bands centered on 443, 551, and 680 nm are used to estimate daily mean photosynthetically available radiation (PAR) at the ice-free ocean surface. The PAR algorithm uses a budget approach, in which the solar irradiance reaching the surface is obtained by subtracting from the irradiance arriving at the top of the atmosphere (known), the irradiance reflected to space (estimated from the EPIC Level 1b radiance data), taking account of atmospheric transmission and surface albedo (modeled). Clear and cloudy regions within a pixel do not need to be distinguished, which dismisses the need for often-arbitrary assumptions about cloudiness distribution within a pixel and is therefore adapted to the relatively large EPIC pixels. A daily mean PAR is estimated on the source grid for each EPIC instantaneous daytime observation, assuming no cloudiness changes during the day, and the individual estimates are remapped and weight-averaged using the cosine of the Sun zenith angle. In the computations, wind speed, surface pressure, and water vapor amount are extracted from NCEP Reanalysis 2 data, aerosol optical thickness and Angström coefficient from MERRA-2 data, and ozone amount from EPIC Level 2 data. Areas contaminated by Sun glint are excluded using a threshold on Sun glint reflectance calculated using wind data. Ice masking is based on NSIDC near-real-time ice fraction data. The product is evaluated against *in situ* measurements at various locations and compared with estimates from sensors in polar and geostationary orbits (MODIS, AHI). Unlike with MODIS, the EPIC PAR product does not exhibit gaps at low and middle latitudes. Accuracy is satisfactory for long-term studies of aquatic photosynthesis, especially given the much larger uncertainties on the fraction of PAR absorbed by live algae and the quantum yield of carbon fixation. The EPIC daily mean PAR product is generated operationally on a Plate Carrée (equal-angle) grid with 18.4 km resolution at the equator and on an 18.4 km equal-area grid, i.e., it is fully compatible with the NASA Greenbelt OBPG ocean-color products. Data are available since the beginning of the DSCOVR mission (i.e., June 2015) from the NASA Langley ASDC website.

Keywords: photosynthetically available radiation, satellite remote sensing, Lagrange L1 orbit, EPIC sensor, DSCOVR mission, light absorption and scattering, ocean biogeochemistry

OPEN ACCESS

Edited by:
Gregory Schuster, National Aeronautics and Space Administration (NASA), United States

Reviewed by:
Chuanfeng Zhao, Beijing Normal University, China
Tamas Varnai, University of Maryland, Baltimore County, United States

****Correspondence:***
Robert Frouin
rfrouin@ucsd.edu

Specialty section:
This article was submitted to Satellite Missions, a section of the journal Frontiers in Remote Sensing

Received: *11 December 2021*
Accepted: *02 March 2022*
Published: *12 April 2022*

Citation:
Frouin R, Tan J, Compiègne M, Ramon D, Sutton M, Murakami H, Antoine D, Send U, Sevadjian J and Vellucci V (2022) The NASA EPIC/DSCOVR Ocean PAR Product. Front. Remote Sens. 3:833340. doi: 10.3389/frsen.2022.833340

1 INTRODUCTION

The solar energy flux reaching the ocean surface in the spectral range 400–700 nm, referred to as photosynthetically available (or active) solar radiation (PAR), controls the rate of photosynthesis by phytoplankton and therefore the development of crustaceans, fish, and other consumers (e.g., Ryther, 1956; Platt et al., 1977; Kirk, 1994; Falkowski and Raven, 1997). It ultimately regulates the composition of marine ecosystems. Sunlight absorbed differentially by the upper ocean affects mixed-layer dynamics and oceanic currents (e.g., Nakamoto et al., 2000, 2001; Murtugudde et al., 2002; Sweeney et al., 2005; Ballabrera-Poy et al., 2007), with local and remote consequences on atmospheric temperature and circulation (e.g., Miller et al., 2003; Shell et al., 2003). Absorption by phytoplankton and other water constituents tend to reduce the planetary albedo, i.e., warm the planet (Frouin and Iacobellis, 2002). Knowing the spatiotemporal distribution of PAR over the oceans is critical to understanding biogeochemical cycles of carbon, nutrients, and oxygen and biological-physical interactions (a major uncertainty in coupled climate models) and, therefore, to addressing important global change issues such as the fate of anthropogenic atmospheric carbon dioxide and making accurate projections of future climate (e.g., Frouin et al., 2018a).

Regional and global maps of PAR at the ocean surface can be obtained from a variety of passive Earth-viewing satellite optical sensors. The sensors operating from geostationary altitude provide adequate temporal sampling to deal with cloud diurnal variability but have degraded spatial resolution at high latitudes, and they only cover part of the oceans, i.e., several sensors, optimally positioned are necessary to provide global coverage. Sensors in polar orbits provide the same spatial resolution at all latitudes but pass less frequently over the same target at middle and low latitudes. For ocean primary productivity computations, it is convenient to estimate both PAR and bio-optical variables (phytoplankton chlorophyll abundance, absorption coefficients) from the same sensor. Ocean-color sensors offer this capability, even though they are principally designed to retrieve water reflectance if they do not saturate over clouds. The same data preprocessing is required, i.e., PAR can be produced with little extra effort as part of the same processing line. In this way, the key variables in primary production modeling are provided together at the same resolution, facilitating studies of photosynthesis and ecosystem dynamics.

In this context, a simple yet efficient and fairly accurate algorithm has been developed to estimate the daily mean PAR at the ocean surface from Sea-viewing Wide Field-of-view Sensor (SeaWiFS) data (Frouin et al., 2003) and adapted for application to MODerate resolution Imaging Spectroradiometer (MODIS) data (Frouin et al., 2012), GLobal Imager (GLI) data (Frouin and Murakami, 2007), GOCI data (Frouin and McPherson, 2013; Kim et al., 2016), Medium Resolution Imaging Spectrometer (MERIS) data, Visible Infrared Imaging Radiometer Suite (VIIRS) data, Second-generation Global Imager (SGLI) data, and Advanced Hiwamari Imager (AHI) data with plans for an extension to future ocean color sensors. Daily mean PAR refers to the 24-h averaged planar quantum energy flux from the Sun in the spectral range 400–700 nm. It is expressed in units of Einstein per meter squared per day, i.e., $Em^{-2}d^{-1}$. The global daily mean PAR products from SeaWiFS, MODIS, VIIRS, and MERIS data have been routinely generated by the National Aeronautics and Space Administration (NASA) Ocean Biology Processing Group (OBPG) and made available to the user community from their website (https://oceancolor.gsfc.nasa.gov). Estimated uncertainty, based on comparisons against *in situ* measurements, expressed in relative root-mean-square (RMS) difference and bias, is typically 10-30% and 4-9%, respectively, depending on satellite sensor and atmospheric conditions (Frouin et al., 2003; Frouin et al., 2012; Laliberté et al., 2016; Ramon et al., 2016; Somayajula et al., 2018). Somayajula et al. (2018) compared satellite-based PAR algorithms used in primary production studies; they concluded that the best overall performance was obtained with the NASA OBPG algorithm. This uncertainty is reasonable for large-scale studies of aquatic photosynthesis (e.g., Frouin et al., 2012; Frouin et al., 2018a), but better accuracy is desirable. Note, in this respect, that primary productivity models depend not only on PAR but also on efficiency factors that are difficult to estimate with uncertainty comparable to (i.e., as low as) that of PAR.

The standard Level-2 and -3 PAR products generated by the NASA OBPG have been used extensively in the science community for a variety of applications. In primary productivity calculations, they have replaced PAR estimates obtained from a clear sky model corrected for cloudiness using fractional cloud coverage or deduced from satellite estimates of total solar irradiance, the treatment applied in Longhurst et al. (1995), Antoine et al. (1996), and Behrenfeld and Falkowski (1997) to obtain the first global maps of seasonal and/or annual oceanic primary productivity from space. Such treatment is limited, because the effect of clouds on PAR does not depend only on fractional coverage, but also on optical thickness, and the relation between total solar irradiance and PAR, rather constant under clear skies (Baker and Frouin, 1987), varies strongly with water vapor and cloud liquid water content (Frouin and Pinker, 1995). Studies using the NASA OBPG PAR products have addressed a variety of topics, including biosphere productivity during an El Niño transition (Behrenfeld et al., 2001), chlorophyll-a and carbon-based ocean productivity modeling (Behrenfeld et al., 2005; Platt et al., 2008), climate-driven trends in productivity (Behrenfeld et al., 2006; Kahru et al., 2009; Henson et al., 2010), phytoplankton class-specific productivity (Uitz et al., 2010), inter-comparison of productivity algorithms (Carr et al., 2006; Lee et al., 2015), and the relation between primary productivity, vertical mixing, and atmospheric input (Tang and Shi, 2012). They have also been used to check the stability of CERES measurements (Loeb et al., 2006).

The parameters governing PAR variability are essentially the Sun zenith angle and the cloud transmittance. Aerosol properties and surface albedo have a smaller impact. Since the Sun zenith angle can be computed precisely, estimating daily PAR from data collected by a single sensor aboard a Sun-synchronous satellite is chiefly limited, in terms of accuracy, by the lack of information

about diurnal variability of cloud properties, especially at low and middle latitudes. This variability may be large in some regions, as evidenced by the International Cloud Climatology Project (ISCCP) cloud analyses (Bergman and Salby, 1996; Rossow and Shiffer, 1999) and other studies (e.g., Wang and Zhao, 2017; Zhao et al., 2019; Yang et al., 2020). Consequently, the PAR products from individual polar-orbiting sensors exhibit biases, not only with respect to ground truth but also between themselves, as evidenced in inter-comparison and evaluation studies (Frouin et al., 2003, 2012; Tan and Frouin, 2019). Merging data from several sensors with different overpass times may significantly improve the quality of daily PAR estimates, as demonstrated with MODIS-Terra, SeaWiFS, and MODIS-Aqua, which cross the equator at approximately 10:30, 12:00, and 13:30 local time (Frouin et al., 2012). In generating a long-term PAR time series, however, one must deal with various sensor combinations, and there is a need, for ocean biogeochemistry studies related to climate change to reduce the individual biases against *in situ* measurements and make the PAR estimates consistent across individual sensors (Frouin et al., 2018a).

The Earth Polychromatic Imaging Camera (EPIC) onboard DSCOVR, operating from the first Sun-Earth Lagrange point (L1) one million miles from Earth (Marshak et al., 2018; https://avdc.gsfc.nasa.gov/pub/DSCOVR/Web_EPIC/), provides a great opportunity to generate accurate PAR products and address issues associated with polar-orbiting sensors. By frequently observing the sunlit part of the Earth, EPIC inherently allows one to account properly for diurnal cloud variability, while maximizing spatial coverage. In other words, EPIC with respect to PAR can do the job of several geostationary sensors with the further advantage that spatial resolution at high latitudes is less of an issue (the L1 orbit is much farther from Earth than the geostationary orbit). The spectral bands centered on 443, 551, and 680 nm, the non-saturation of measured radiance over clouds, and the spatial resolution of 10 km at nadir are adequate for PAR calculations, especially using the NASA OBPG algorithm, which does not require knowing whether the pixel is clear or cloudy, i.e., is applicable to large pixels.

In view of the above, the current NASA OBPG daily mean PAR algorithm has been modified/adapted for application to EPIC data. Algorithm uncertainties have been associated with EPIC PAR estimates on a pixel-by-pixel basis. A full processing line has been created and implemented to generate operationally daily mean EPIC PAR products at the NASA Center for Climate Simulation (NCCS). The data are archived at and distributed by the Langley Atmospheric Science Data Center (ASDC). In **Section 2**, the methodology to estimate daily mean PAR from EPIC data is presented and the various steps to obtain the surface flux values are detailed. The tasks include integrating atmospheric functions spectrally and temporally during the day (the number of observations in a day varies depending on geographic location), eliminating data contaminated by Sun glint, incorporating ancillary information such as ozone content, sea ice extent (for masking), and aerosol optical properties, and remapping the data to a common grid. In **Section 3**, a procedure is described to associate algorithm uncertainties (i.e., bias and standard deviation) to each EPIC daily mean PAR estimate as a function of parameters readily available from applying the algorithm, i.e., daily mean clear sky PAR and cloud factor (characterizes the effect of clouds on daily mean PAR). In **Section 4**, EPIC PAR estimates are compared to *in situ* measurements routinely collected from long-term fixed buoys. Experimental performance is also compared to that of MODIS PAR estimates. In **Section 5**, examples of global daily mean PAR products are displayed and examined in view of corresponding MODIS and AHI products, and PAR time series at contrasted locations are presented to illustrate the capability of EPIC to describe PAR seasonal to interannual variability. In **Section 6**, finally, the EPIC PAR algorithm and its performance against field data and other satellite estimates are summarized, advantages and limitations of using observations from the L1 orbit are pointed out, the significance of the new ocean PAR product in complementing existing PAR time series for a wide range of research applications is emphasized, and a perspective for future work to estimate variables used more directly in primary productivity or water reflectance models, such as scalar PAR, spectral PAR, and average cosine of the light field just below the surface, as well as ultraviolet fluxes, is provided.

2 ALGORITHM DESCRIPTION

The algorithm estimates daily mean PAR reaching the ice-free ocean surface, as defined above. Following Frouin et al. (2003), a budget approach is used, in which the solar flux reaching the surface is obtained by subtracting from the flux arriving at the top of the atmosphere (know) the flux reflected to space (estimated from the EPIC measurements) accounting for atmospheric transmission and surface albedo (modeled). Clear and cloudy regions within a pixel do not need to be distinguished, which is appropriate to the relatively large (i.e., 10 km at nadir) EPIC pixels. This approach was shown to be valid by Dedieu et al. (1987) and Frouin and Chertock (1992).

Based on the previous work, the PAR model assumes that the effects of clouds and other atmospheric constituents are decoupled. The planetary atmosphere is therefore modeled as a clear sky layer that contains molecules and aerosols positioned above a cloud/surface layer, and surface PAR is expressed as the product of a clear-sky component and a transmittance that accounts for cloudiness and surface optical effects. Under solar incidence (zenith angle) θ_s, the incoming spectral solar flux at the top of the atmosphere, $E_{TOA}cos(\theta_s)$, is reduced by a factor $T_a(\theta_s)T_g(\theta_s)[1 - S_aA(\theta_s)]^{-1}$ by the time it enters the cloud/surface system, where T_a is the clear-sky transmittance (due to scattering by molecules and aerosols), T_g is the gaseous transmittance (essentially due to absorption by ozone), S_a is the spherical albedo of the clear atmosphere, and A is the cloud/surface system albedo. As the transmitted flux, $E_{TOA}cos(\theta_s)T_a(\theta_s)T_g(\theta_s)[1 - S_aA(\theta_s)]^{-1}$, passes through the cloud/surface system, it is further reduced by a factor $1—A$. The instantaneous planar flux reaching the ocean surface at any wavelength in the PAR spectral range, E, is then given by:

$$E(\theta_s) = E_0(\theta_s)[1 - A(\theta_s)][1 - A_s(\theta_s)]^{-1}[1 - S_a A(\theta_s)]^{-1}, \quad (1)$$

where A_s is the albedo of the ocean (surface and water body) and $E_0(\theta_s) = E_{TOA} cos(\theta_s) T_a(\theta_s) T_g(\theta_s)$ is the solar flux that would reach the surface if the cloud layer and the surface were non-reflecting. In clear sky conditions, A reduces to A_s and E to $E_{clear} = E_0(1 - S_a A_s)^{-1}$. The term $[1 - S_a A(\theta_s)]^{-1}$ in **Eq. 1** represents interactions between the cloud/surface layer and the clear atmosphere.

To compute E, A is expressed as a function of the radiance measured by EPIC in bands centered on 443, 551, and 680 nm, and this for each observation collected during the day (i.e., between sunrise and sunset). These bands do not saturate over clouds, and they sample sufficiently the PAR spectral range. In this range, the scattering properties of molecules and aerosols vary smoothly with wavelength, gaseous absorption is relatively weak, and A is quite constant spectrally. The algorithm works on a pixel-by-pixel basis, i.e., a daily mean PAR estimate is obtained for each pixel of the satellite imagery. The various processing steps and procedures are detailed in the following.

First the bidirectional reflectance of the cloud/surface layer, ρ, is determined from the instantaneous EPIC Level 1b reflectance data at source resolution. This is only accomplished for pixels that are not contaminated by sea ice or Sun glint. For sea ice masking, fractional ice coverage at 25 km resolution from the National Snow and Ice Data Center (NSIDC) is used. If the fractional coverage is greater than 0.1, then the pixel is discarded. For Sun glint masking, the Fresnel signal at the wavy interface surface is calculated from the wind speed according to Cox and Munk (1954), and all pixels with a glint reflectance above 0.05 at 780 nm are eliminated. National Centers for Environmental Prediction (NCEP) Reanalysis-2 wind data at 1° and 6-h resolution is used after interpolation to the EPIC observation time. Both ancillary data sets are remapped to the source grid prior to masking. Since in the modeling the clear atmosphere is located above the cloud/surface layer, ρ is obtained from the top-of-atmosphere (TOA) reflectance, ρ_{TOA} by inverting the following equation (Tanré et al., 1979):

$$\rho_{TOA}(\theta_s, \theta_v, \phi) = T_g(\theta_s, \theta_v)\left[\rho_a(\theta_s, \theta_v, \phi) + \rho T_a(\theta_s, \theta_v)(1 - S_a\rho)^{-1}\right], \quad (2)$$

where ρ_a is atmospheric reflectance and θ_v and ϕ are view zenith and relative azimuth angles, respectively. In **Eq. 2** T_g and T_a are transmittances along the Sun-to-surface and surface-to-sensor path. This expression is strictly valid for an isotropic target of reflectance ρ, which is not the case for the cloud/surface layer, but a good approximation for many geometries, except when θ_s is large and clouds are optically thin, i.e., when the albedo of that layer, A, is relatively close to ρ (Zege, et al., 1991). At large θ_s, however, E becomes small since modulated directly by $cos(\theta_s)$, and when clouds are thin their impact on $(1 - A)$ in **Eq. 1** is also small, which tends to minimize effects on daily mean surface fluxes. A better treatment would be to use the following equation (Tanré et al., 1979; Deschamps et al., 1983):

$$\rho_{TOA}(\theta_s, \theta_v, \phi) = T_g(\theta_s, \theta_v)\{\rho_a + [\rho(\theta_s, \theta_v, \phi) - A(\theta_s)]e^{-\tau_a m} + A(\theta_s)T_a(\theta_s, \theta_v)[1 - S_a A(\theta_s)]^{-1}\}, \quad (3)$$

where τ_a is the optical thickness of the clear atmosphere and m is airmass, i.e., $m = 1/\cos(\theta_s) + 1/\cos(\theta_v)$. **Eq. 3** reduces to **Eq. 2** when ρ is isotropic. The retrieval of ρ would be accomplished through iteration. This would require a first estimate of A, which can be obtained as described below for isotropic ρ.

To compute the atmospheric functions T_g, T_a, and ρ_a, the surface pressure and water vapor amount are extracted from NCEP Reanalysis 2 data, aerosol optical thickness at 550 nm, Angström coefficient, and single scattering albedo at 550 nm from MERRA-2 data at 0.625° × 0.5° (Gelaro et al., 2017), and ozone amount from EPIC Level 2 data at source resolution (Herman et al., 2018). Single scattering albedo is assumed constant over the PAR spectral range. For ρ_a, the quasi-single scattering approximation (Q-SSA) used in Frouin et al. (2003), which gives too high values at large zenith angles, is replaced by a parameterization that combines Q-SSA and exact single-scattering approximation (SSA):

$$\rho_a = f_{SSA}(m, \tau_{aer})\rho_a(SSA) + f_{Q\text{-}SSA}(m, \tau_{aer})\rho_a(Q\text{–}SSA), \quad (4)$$

where f_{SSA} and $f_{Q\text{–}SSA}$ depend on m and aerosol optical thickness, τ_{aer}, but are independent of the aerosol model. These functions were obtained from the simulations with the 6S code (Kotchenova et al., 2006, 2007) for atmospheres containing various mixtures of maritime and continental aerosols and angular geometries. **Figure 1** displays ρ_a at 443, 551, and 680 nm as a function of θ_v for θ_s = 70°. Scattering angle, quasi constant with EPIC, is fixed at 171.5°. The aerosols are of maritime type and τ_{aer} at 550 nm is 0.2 and 0.4 (top and bottom panels, respectively). The parameterization works well yielding ρ_a values very close to the 6S values except in the blue, where τ_{aer} is large (0.4) and the molecular scattering is effective. At 443 nm the coupling between aerosol and molecule scattering is relatively important and the 6S ρ_a is substantially smaller than ρ_a(Q–SSA), even at θ_v < 65°, which is partly explained by the fact that in Q-SSA the molecule and aerosol contributions to atmospheric reflectance correspond to the atmosphere containing only molecules or aerosols, i.e., the neglected aerosol-coupling term is negative (Deschamps et al., 1983). The 6S and SSA values are quite similar at that wavelength, a consequence of the SSA formulation that also assumes either molecules or aerosols, i.e., the probability of encountering one type of scatterer is enhanced (SSA values are expected to be lower in the presence of both molecules and aerosols). As wavelength increases, this effect is less prominent because the atmosphere is less thick optically contributing to larger differences between 6S and SSA values.

Once the reflectance of the cloud/surface layer, ρ, is determined, it is converted into albedo A. This is accomplished for each observation during daytime and the three spectral bands by applying a cloud bidirectional correction factor F (independent of wavelength) to $\rho - A_s$ since $A \approx NAc + A_s$ where Ac is cloud albedo and N is

fractional cloud cover (see Frouin and Chertock, 1992; Frouin et al., 2003), i.e.,

$$A = F(\rho - A_s) + A_s, \tag{5}$$

Analytical formulas developed by Zege et al. (1991) for optically thick scattering layers in the non-absorbing medium are used for F. The parameterization depends on the asymmetry coefficient of the cloud indicatrix, g, and the cloud optical thickness, τ_c, which are fixed at 0.853 and 15, respectively. Sensitivity of F on g and τ_c is an issue, especially when τ_c is relatively small (ρ exhibits more directionality), but since E depends on (1 – A) the relative impact on E computed from **Eq. 1** is reduced in such situations (A is also small). The g and τ_c variables can be viewed as tuning parameters, e.g., to reduce biases in estimated fluxes. The surface albedo A_s is parameterized as a function of the Sun zenith angle, aerosol optical thickness at 500 nm, and wind speed following Jin et al. (2004). In the A_s calculation, the chlorophyll-a concentration is fixed at 0.1 mgm^{-3}, and the wind speed is from NCEP Reanalysis-2 data.

Next, the daily mean PAR, $< E_{PAR} >$, is computed by integrating over the PAR spectral range, i.e., 400 to 700 nm, and the length of the day:

$$< E_{PAR} > = \left(\frac{1}{24}\right) \int_t [cos(\theta_s(t))G(t)]dt$$
$$\text{with } G = \int_\lambda \left[E_{TOA} T_g T_a (1-A)(1 - A_s)^{-1}(1 - S_a A)^{-1}\right]d\lambda, \tag{6}$$

where E_{TOA} is the extraterrestrial spectral solar flux per unit of wavelength corrected for Earth-Sun distance variation during the year and time t is expressed in hour. The integral is calculated for each EPIC observation during the day. In other words, if after masking a surface target (pixel) is observed n times during the day, the algorithm generates n daily mean PAR values. The dependence of A and A_s on θ_s is accounted for in the time integration, but assuming that the characteristics of the atmosphere and surface are unchanged during the day. This is a crude assumption, especially for cloudiness, but diurnal variability of the atmosphere is considered implicitly in the final step of the algorithm (see below).

In the final step, the individual daily mean estimates obtained on the source grid (number varies from 1 to 13 depending on geographical location, the time during the year, and data availability) are first remapped to an 18.4 km equal-area grid and weight-averaged using the cosine of the Sun zenith angle and then remapped to a Plate Carrée (equal-angle) grid with 18.4 km resolution at the equator. The remapping algorithm is exactly the one used by NASA OBPG to generate a Level 3 binned ocean color products (https://oceancolor.gsfc.bnasa/gov/docs/format/l3bins). Triangular-based linear interpolation is used to fill missing pixels at the edges.

The weighting procedure to obtain the final $< E_{PAR} >$ estimates is accurate, except when only one or two EPIC observations per day is available. Such situations are infrequent; they are due to instrument problems and mission activities (e.g., sensor calibration, spacecraft maneuvers). The accuracy of the weighting procedure was checked from radiative transfer calculations with hourly MERRA-2 data for

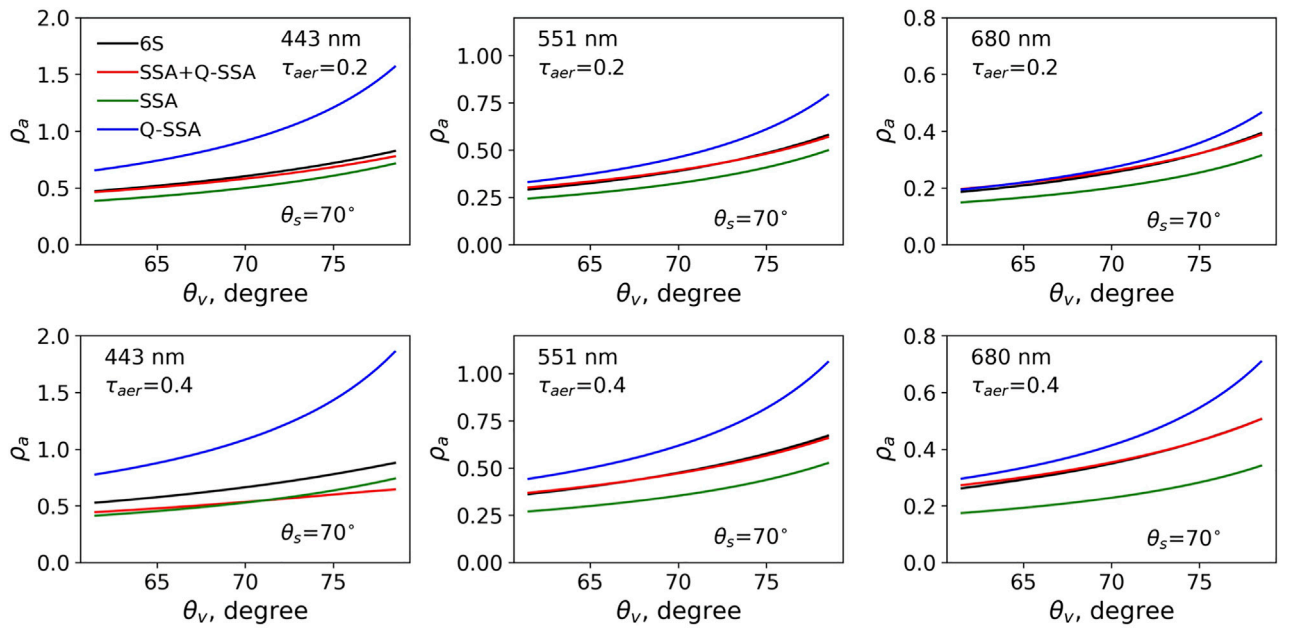

FIGURE 1 | Atmospheric reflectance ρ_a parameterization using SSA, Q-SSA, and a combination of SSA and Q-SSA (green, blue, and black dots, respectively). 6S calculations (RT) are displayed as red curves. Sun zenith angle is 70 deg., scattering angle is 171.5 deg., aerosols are of maritime type with optical thickness of 0.2 and 0.4 at 550 nm, and wavelengths are 388, 551, and 680 nm.

cloud and aerosol properties and ozone and water vapor contents. In the calculations, E_{PAR} was expressed as $E_{PAR} = E_{clearPAR}(1 - NA_c)$, where A_c is obtained from τ_c according to Fitzpatrick et al. (2004) and $E_{clearPAR}$ is simulated with the 6S code assuming a chlorophyll-a concentration of 0.5 mgm^{-3} and a wind speed of 5 ms^{-1}. Two dates, i.e., January 1 and July 1, 2018, and ocean locations evenly distributed in the spatial domain within 60°S to 40°N and 180°W to 180°E, i.e., every 5° along latitude, and every 6.25° along longitude, were selected. **Table 1** displays the comparison statistics of $\cos(\theta_s)$-weighed $< E_{PAR} >$ obtained from 1, 2, 3, 6, 9, and 12 individual $< E_{PAR} >$ estimates during the day versus the $< E_{PAR} >$ value obtained by trapezoidal integration of all the hourly E_{PAR} values at the time of the MERRA-2 observations (referred to as actual or theoretical $< E_{PAR} >$). The individual estimates correspond to hourly observations randomly distributed between sunrise and sunset. In estimating $< E_{PAR} >$ for each observation, the aerosol and cloud properties and gaseous absorber amounts are assumed unchanged during the day, but the dependence of A_c and A_s on θ_s are accounted for in the time integration, as in the EPIC daily mean PAR algorithm. The $\cos(\theta_s)$-weighted $< E_{PAR} >$ values agree well with the theoretical ones when 3 and more observations per day are used, with biases less than 0.10 (0.4%) $Em^{-2}d^{-1}$ in magnitude and root-mean-square difference (RMSD) less than 3.83 (14.2%) $Em^{-2}d^{-1}$. RMSD is reduced to 1.34 (4.5%) and 1.07 (3%) $Em^{-2}d^{-1}$ with 9 and 12 observations per day. The biases are small because of the random sampling of times during the day and the large number of locations considered in the data ensemble. RMSD is noticeably larger when 1 or 2 $< E_{PAR} >$ estimates are used, i.e., 7.00 (25.9%) and 4.86 (18.0%) $Em^{-2}d^{-1}$, respectively. In such situations, the alternative procedure to obtain $< E_{PAR} >$, i.e., trapezoidal integration of hourly E_{PAR} values, would also give inaccurate results.

A way to reduce the sampling biases in such situations, not yet implemented in the algorithm, is to use MERRA-2 hourly cloud products for the very day of the EPIC observations, as proposed by Tan et al. (2020). If τ_{cMERRA} and N_{MERRA} denote the MERRA-2 cloud optical thickness and fractional coverage, A is replaced by A' in **Eq. 5** as follows:

$$A' = (A - A_s)[N_{MERRA}(t)A_c(\tau_{cMERRA}(t))] \Big/ \times [N_{MERRA}(t_i)A_c(\tau_{cMERRA}(t_i))] + A_s, \quad (7)$$

where t_i is the time of satellite observation and A_c is computed from τ_{cMERRA} at time t and t_i. Basically, the quantity $A - A_s$ is adjusted by the ratio of NA_c computed from MERRA-2 products at times t and t_i In **Eq. 6** A, determined at t_i, is corrected for variations with θ_s, but assuming that cloud properties are unchanged. **Figure 2** illustrates the potential improvement expected using **Eq. 6**. It displays scatter plots of OBPG MODIS-A $< E_{PAR} >$ estimates at source resolution (about 1 km) versus *in situ* measurements at the Chesapeake Bay CERES Ocean Validation Experiment (COVE) site (36.9°N, 75.7°W) in the Western Atlantic during 2003–2014 (see Tan et al., 2020, for details about the *in situ* data collected at that site). Bias is reduced from 1.72 (5.3%) to −0.05 (-0.1%) $Em^{-2}d^{-1}$, i.e., practically eliminated on average, but RMSD is marginally improved, i.e., 7.02 (21.4%) instead of 7.37 (22.5%) $Em^{-2}d^{-1}$, when using the hourly MERRA-2 cloud products.

3 UNCERTAINTY ASSIGNMENT

Associating uncertainty to each $< E_{PAR} >$ estimate is necessary to use properly the information provided by the estimate. It allows one to verify that variability and trends are actual to merge different datasets optimally, and to constrain adequately model predictions (Frouin et al., 2018a; IOCCG, 2019). Comparisons with contemporaneous and collocated *in situ* measurements at a few sites, the current approach to quantify experimental performance may not be sufficient to describe uncertainty in the wide range of conditions expected to be encountered. Representing uncertainty on a pixel-by-pixel basis requires modeling the measurement, identifying all possible error sources (e.g., noise in the input variables, imperfect or incomplete mathematical model), and determining the combined uncertainty (JGCM-100, 2008; Povey and Grainger, 2015; IOCCG, 2019). Algorithm uncertainty is due to model approximations and parameter errors (e.g., using plane-parallel atmosphere, decoupling effects of clouds and clear atmosphere, neglecting diurnal variability of clouds, fixing cloud optical thickness to a constant in bidirectional correction) if the input variables (EPIC TOA reflectance at wavelengths in the PAR spectral range) are known perfectly. A complete pixel-by-pixel uncertainty budget should include, not only algorithm uncertainty, but also uncertainty due to measurement noise,

TABLE 1 | Statistics of comparing $cos(\theta_s)$-weighted $< E_{PAR} >$ with actual (theoretical) $< E_{PAR} >$ using different number of observations at randomly distributed hourly times during the day on January 1 and July 1, 2018, at ocean locations within 60°S to 40°N and 180°W to 180°E. The number of data points (*N*) is slightly different when six and more hourly observations per day are used, because such number of observations may not be available for some locations during some days of the year.

No. of observations	R^2	Bias ($Em^{-2}d^{-1}$)	RMSD ($Em^{-2}d^{-1}$)	N
1	0.859	−0.07 (−0.3%)	7.00 (25.9%)	1,874
2	0.929	0.04 (0.1%)	4.86 (18.0%)	1,874
3	0.955	−0.10 (−0.4%)	3.83 (14.2%)	1,874
6	0.987	0.06 (0.2%)	2.04 (7.4%)	1,851
9	0.993	−0.02 (−0.1%)	1.34 (4.5%)	1,682
12	0.996	−0.06 (−0.2%)	1.07 (3.0%)	1,095

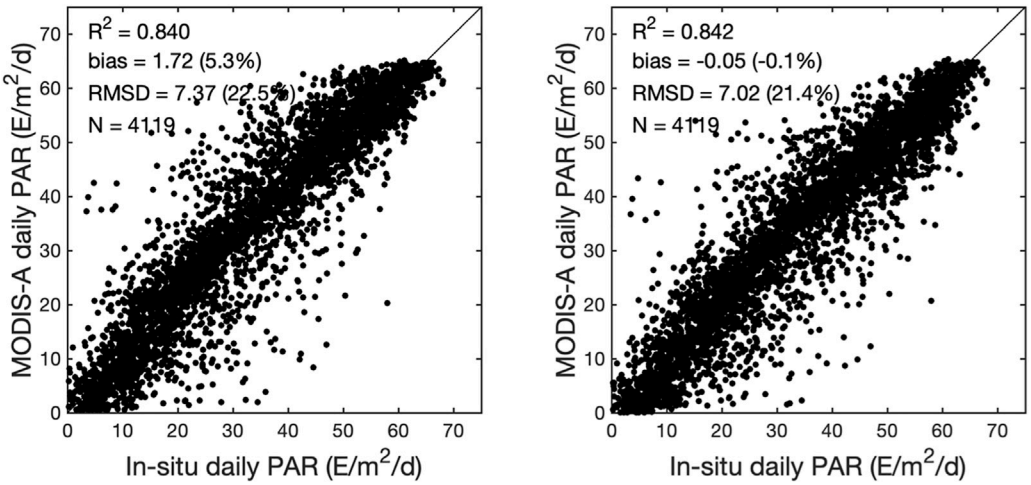

FIGURE 2 | MODIS-A $<E_{PAR}>$ estimate vs. *in situ* data collected at the COVE site in the Western Atlantic. Left: No correction for cloud diurnal variability. Right: Using MERRA-2 hourly cloud products.

radiometric calibration, and preprocessing to Level 1b, a component that is difficult to determine accurately.

The procedure described in Frouin et al. (2018a, b) is used to estimate and provide, for each pixel of the daily mean PAR product, the algorithm uncertainty component of the total uncertainty budget, which is expected to dominate. The bias and standard deviation portions are calculated as a function of clear sky daily mean PAR, $<E_{clearPAR}>$, and cloud factor, $<CF_{PAR}> = <E_{PAR}>/<E_{clearPAR}>$ (characterizes the effect of clouds on PAR and varies from 0 to 1), by simulating for many situations the satellite measurements and corresponding $<E_{PAR}>$ and comparing the latter to the $<E_{PAR}>$ estimated from the TOA reflectance. The simulations were performed with the Atmospheric Radiative Transfer Database for Earth and Climate Observation (ARTDECO) code (Dubuisson et al., 2016; https://www.icare.univ-lille.fr/artdeco/) using as input several years (2003 to 2012) of MERRA-2 hourly data (aerosol and cloud properties). The large number of data points allows one to sample a wide range of geometric configurations for the satellite data and atmospheric variability, in particular many situations of daytime nebulosity for all latitudes. At this stage, the resulting look-up-tables (LUTs) only depend on $<E_{clearPAR}>$ and $<CF_{PAR}>$, but other parameters, e.g., angular geometry and latitude, will be considered in the future. Since the final $<E_{PAR}>$ is a $\cos(\theta_s)$-weighted average of individual $<E_{PAR}>$ estimates during the day, the uncertainty on the final $<E_{PAR}>$ is obtained by weighting the individual uncertainties in the same way.

Figure 3 displays the resulting uncertainty (bias and standard deviation) on individual $<E_{PAR}>$ estimates as a function of $<CF_{PAR}>$ for several $<E_{clearPAR}>$ levels, i.e., 12, 35, and 58 $\mathrm{Em^{-2}d^{-1}}$. The bias between estimated and simulated

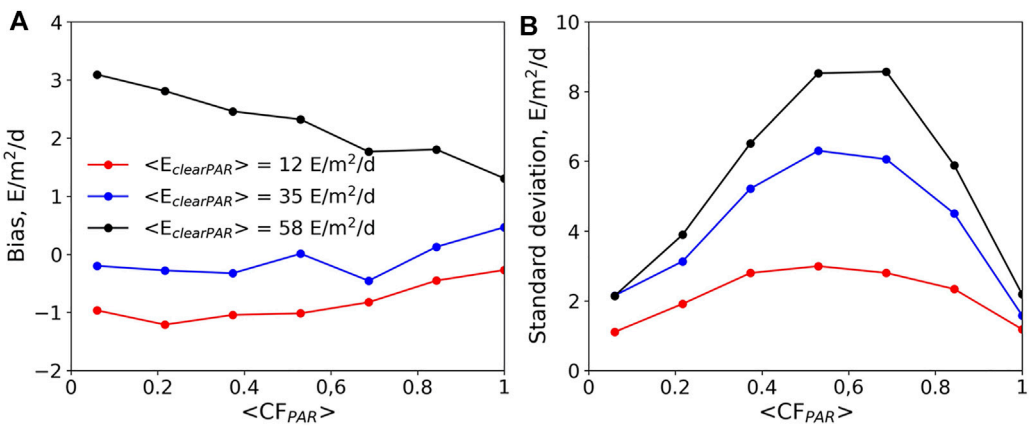

FIGURE 3 | Algorithm uncertainty on individual $<E_{PAR}>$ estimates (i.e., using one observation per day) as a function of $<CF_{PAR}>$ for several values of $<E_{clearPAR}>$. **(A)** Bias (estimated minus simulated values); **(B)** standard deviation. The theoritical uncertainty was obtained from simulations of the TOA reflectance and $<E_{PAR}>$for a wide range of situations using 10 years of MERRA-2 aerosol and cloud data (see text for details).

TABLE 2 | I Characteristics of the *in situ* above surface downward solar irradiance datasets used in the evaluation of the EPIC $< E_{PAR} >$ estimates.

Sites	Geographic location	Platform type	Sensor type	Time period	Measurement frequency (min)
BOUSSOLE	43.3667°N, 7.9°E	Moored buoy	PAR (400-700 nm)	5/29/2015–7/28/2019	15
CCE-1	33.462°N, 122.526°W	Moored buoy	Multispectral (412 nm, 443 nm, 490 nm, 510 nm, 555 nm, 620 nm, 669 nm)	10/18/2018–6/9/2020	30
CCE-2	34.309°N, 120.804°W	Moored buoy	Multispectral (412 nm, 443 nm, 490 nm, 510 nm, 555 nm, 620 nm, 669 nm)	8/15/2017–9/8/2020	30

$< E_{PAR} >$ values (**Figure 3A**) is small (mostly within 1 $\mathrm{Em^{-2}d^{-1}}$ in magnitude) and does not vary much with $< CF_{PAR} >$ at low and moderate $< E_{clearPAR} >$ values (blue and red curves) but reaches 3 $\mathrm{Em^{-2}d^{-1}}$ at high $< E_{clearPAR} >$ values when $< CF_{PAR} >$ is small (black curve). The standard deviation (**Figure 3B**) is peaked toward intermediate cloud factors (the risk or probability that cloudiness at the time of satellite measurement may not be representative of the conditions at other times during the day is larger), increasing from about 2.2 to 8.7 $\mathrm{Em^{-2}d^{-1}}$ when $< E_{clearPAR} >$ increases from 12 to 58 $\mathrm{Em^{-2}d^{-1}}$ and $< CF_{PAR} > = 0.5$, i.e., about 15% relatively.

As mentioned above, a complete per-pixel uncertainty budget must include errors in the Level 1b data, which may require estimating the sensitivity of $< E_{PAR} >$ to input reflectance and the covariance in the various spectral bands (JGCM-100, 2008). Noise in the input data is difficult to estimate, especially spectral correlations, but this can be attempted by analyzing the Level 1b imagery using structure functions or variograms (e.g., Curran and Dungan, 1989; Wald, 1989) and considering information gleaned from inflight calibration studies. The approach, therefore, would be to establish the uncertainty LUTs using noisy TOA reflectance simulations. Note, however, that in the case of MERIS comparisons with match-up data at the COVE site have revealed that experimental uncertainties are similar to algorithm uncertainties obtained from modeled data without noise (Frouin et al., 2018b). Similar results are expected for EPIC $< E_{PAR} >$ uncertainties.

4 EVALUATION AGAINST *IN SITU* MEASUREMENTS

4.1 Datasets

The EPIC $< E_{PAR} >$ product has been evaluated against *in situ* measurements at three mid-latitude oceanic sites (**Figure 4**), where long-term E measurements are routinely acquired from moored buoys i.e., BOUée pour l'acquiSition d'une Série Optique à Long termE (BOUSSOLE) and California Current Ecosystem (CCE) buoys 1 and 2 (hereafter denoted CCE-1 and CCE-2). **Table 2** lists the main characteristics of the data sets. Although situations for which Sun zenith angles stay large during the day (such as in polar regions) were not sampled, the atmospheric conditions at the three sites exhibited large variability in cloud and aerosol properties making the datasets appropriate for statistically quantifying uncertainties in the $< E_{PAR} >$ estimates.

The BOUSSOLE above-surface downward solar irradiance dataset (http://www.obs-vlfr.fr/Boussole/html/project/boussole.php; Antoine et al., 2008) consists of high frequency E_{PAR} measurements (every 15 min) collected from the long-term mooring located at 43.37°N and 7.90°E in the Western Mediterranean Sea about 60 km off the coast (between Nice and Corsica, France). The E_{PAR} measurements were made by Satlantic cosine radiometers installed on top of the immerged part of the buoy during May 29, 2015-July 28, 2019 (i.e., corresponding to the EPIC operational phase). Four deployments were made during this period, but there was a large data gap between December 11, 2017 and February 16, 2019. Before conversion into geophysical quantities, the raw data were calibrated using coefficients provided by the manufacturer and checked for outliers. The E_{PAR} measurements were corrected for tilt effects according to Antoine et al. (2008). To obtain daily mean values, i.e., $< E_{PAR} >$, instantaneous E_{PAR} with tilt angles less than 20° was integrated over time from sunrise to sunset.

The CCE-1 and -2 datasets were collected at two surface moorings in the California Current (http://mooring.ucsd.edu/cce/). Multiple deployments are available and for this study we used the CCE-1 deployments from October 23, 2017 to June 9, 2020, and the CCE-2 deployments from August 15, 2017 to May 7, 2019. CCE-1 is located at 33.46°N, 122.53°W in the core of California Current, approximately 220 km off Point Conception, California. The CCE-2 mooring is operated at 34.31°N and 120.80°W and closer to the shore, approximately 35 km off Point Conception. For both mooring locations, the E measurements were made every 30 min at 412 nm, 443 nm, 490 nm, 510 nm, 555 nm, 620 nm, and 669 nm by Sea-Bird OCR-507 sensors. The raw data were calibrated to actual E using radiative transfer (RT) simulations. First, clear sky days were identified by carefully examining the shape of raw data as a function of time each day. Only those following strictly the cosine function $E_{PAR} = a\cos(\theta_s)e^{-\beta/\cos(\theta_s)}$ with limited error (Tan et al., 2020, **Section 4.1**) were selected. Second, the theoretical E for these clear days were simulated using the 6S code with aerosol properties, water vapor, and ozone, wind speed, and chlorophyll-a concentration from NASA OBPG MODerate resolution Imaging Spectroradiometer (MODIS) and Visible Infrared Imaging Radiometer Suite (VIIRS) Level 2 products. Only days with τ_{aer} less than 0.1 at 550 nm were retained and θ_s was limited to 60°. For those τ_{aer} and θ_s conditions the aerosol transmittance, about $1 - 0.16\tau_{aer}/cos(\theta_s)$ according to Tanré et al. (1979), is above 0.97, i.e., aerosols affect minimally E. Third, linear relations

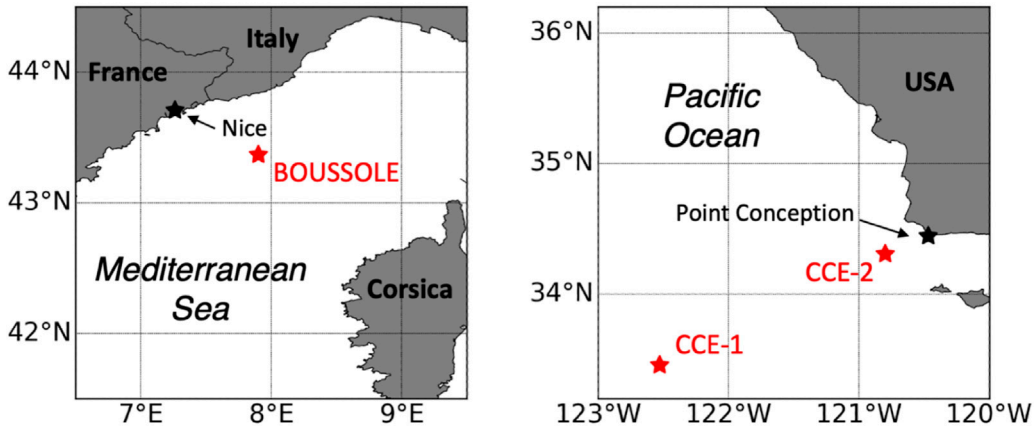

FIGURE 4 | Location of the three *in situ* sites (BOUSSOLE in the Western Mediterranean Sea and CCE-1 and -2 in the Northeast Pacific Ocean) used to evaluate EPIC $<E_{PAR}>$ estimates.

$y = ax$ were determined by comparing the simulated E and raw data yielding the calibration coefficients to be applied to the raw counts. This was done for each deployment since instruments were switched for different deployments and it is expected that the calibration coefficients are different. The raw data corresponding to tilt larger than 10^{o} were not used in this process and dark subtraction was performed before running the linear regression.

Figure 5 displays calibration results at wavelengths 443, 555, and 669 nm for selected deployments. Uncertainty of the calibration gain a (expressed in 10^{-6}/Count) associated with the least-squares fit varies from ± 0.25% to ±0.68% depending on wavelength. Finally, the calibrated spectral E data were first integrated over wavelength and then over time during the day to generate $< E_{PAR} >$.

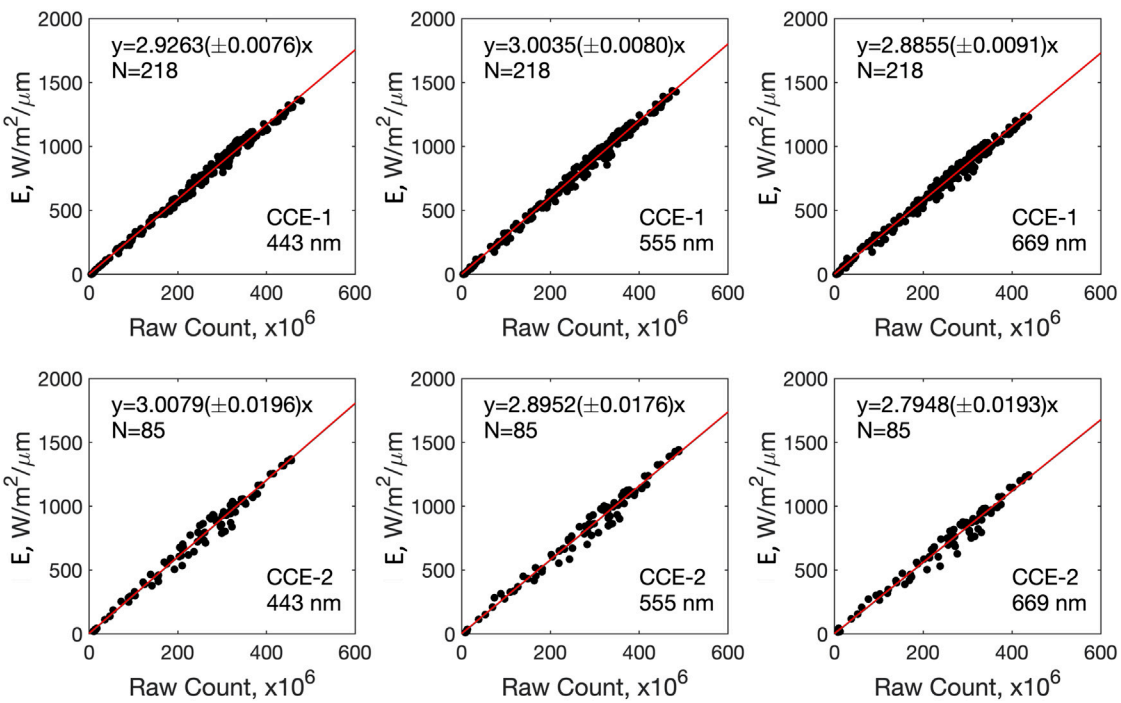

FIGURE 5 | Examples of derived calibration coefficients for CCE-1 (deployment #13) and CCE-2 (deployment #9) datasets at 443, 559, and 669 nm. Raw counts are compared with E simulation in conditions of clear sky with small aerosol optical thickness (see text for details).

4.2 Calibration and Adjustment

The calibrated datasets need to be checked and eventual biases removed before evaluating the EPIC $< E_{PAR} >$ estimates. This is important because laboratory calibration errors and other errors (e.g., due to exposure to the marine environment and data processing) may significantly affect the quality of the *in situ* measurement. An independent check-of-calibration can be performed, as indicated above, by comparing the calibrated measurements to RT simulations in clear sky conditions that allow accurate computations of the atmospheric transmittance. Since the CCE-1 and -2 datasets were already calibrated using such RT simulations, as described in the previous sub-section, no further bias adjustment is necessary for those datasets.

The BOUSSOLE dataset, however, was checked against 6S simulations. The same procedure as described for CCE-1 and -2 datasets, including the selection of clear sky days with small aerosol content and θ_s less than 60°, was used. Only five suitable clear sky days were identified during deployments #3 (June 29, 2016—May 24, 2017) and #5 (February 16, 2019—July 28, 2019); the processing, therefore, was limited to those deployments. Corrections were then applied to the *in situ* data based on the best linear fits ($y = ax$) obtained by regressing, for each deployment separately, instantaneous E simulations against corresponding *in situ* measurements.

Figure 6 displays scatter plots of 6S-simulated versus measured E for the two BOUSSOLE deployments before and after correction. The overall bias before correction (**Figure 6**, left) decreased from 0.55 Em^{-2} d^{-1} (0.4%) to -0.14 Em^{-2} d^{-1} (−0.1%) after correction (**Figure 6**, right) and RMSD from 2.07 Em^{-2} d^{-1} (1.6%) to 1.69 Em^{-2} d^{-1} (1.3%). The small bias and RMSD in the BOUSSOLE data before correction indicate that the BOUSSOLE data are well-calibrated for those deployments and suggests that one may use with confidence the data from other deployments, even without adjustment. Examination of those deployments, however, revealed abnormal E values. Therefore, only data from deployments 3 and 5 were used, and for consistency with the CCE-1 and -2 datasets the small bias adjustment was still applied to the data.

4.3 Match-Up Comparison

EPIC $< E_{PAR} >$ estimates remapped at 18.4 km spatial resolution (equal-area grid) were matched with *in situ* measurements at the three evaluation sites. The EPIC pixel with center closest to the site was selected. One may wonder whether, due to the size of the EPIC $< E_{PAR} >$ pixel, satellite estimates are mismatched with the local *in situ* measurements. Comparisons of MODIS-Aqua and -Terra $< E_{PAR} >$ estimates at 4.6, 9.2, and 18.4 km resolution during June 13, 2015 (beginning of the EPIC dataset), to June 23, 2021, indicated practically no biases at the BOUSSOLE and CCE-1 sites and a slight overestimation by about 0.5–0.7% at 18.4 km resolution with respect to 9.2 and 4.6 km resolution, respectively, at the CCE-2 site. RMSD was 3.9–4.7% between estimates at 9.2 and 18.4 km resolution depending on site and sensor, increasing to 5.6–6.8% between estimates at 4.6 and 18.4 km resolution. In other words, the relatively large spatial resolution of the EPIC pixels is expected to minimally affect statistical performance in terms of bias at the three sites, but RMSD might be significantly underestimated.

Figure 7 displays for each site scatter plots of EPIC, MODIS-Aqua, and MODIS-Terra PAR estimates versus *in situ* measurements. In the comparisons, MODIS values at 9.2 km resolution were averaged to the 18.4 km resolution. The satellite estimates agree with the measurements, but statistical performance is better using EPIC, with bias and RMSD of 0.12 $Em^{-2}d^{-1}$ (0.4%) and 3.93 $Em^{-2}d^{-1}$ (12.0%) for BOUSSOLE, -0.5 $Em^{-2}d^{-1}$ (−1.5%) and 3.4 $Em^{-2}d^{-1}$ (10.2%) for CCE-1, and 0.8 $Em^{-2}d^{-1}$ (2.2%) and 4.6 $Em^{-2}d^{-1}$ (13.3%) for CCE-2. The MODIS-Aqua and -Terra estimates are more biased and exhibit more scatter, reflecting the points made above about using one instead of multiple observations during the day. In particular, the positive bias obtained with MODIS data is likely due to a higher probability of having clear skies at the time of

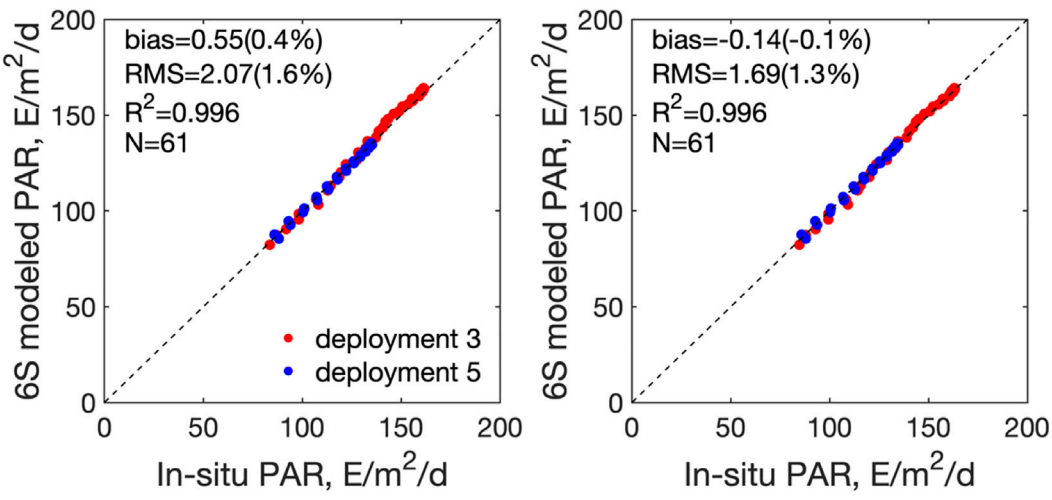

FIGURE 6 | Comparison between 6S-modeled and field-measured instantaneous $<E_{PAR}>$ in very clear sky conditions at the BOUSSOLE site using hourly data: (Left) before any correction; (Right) after adjustment of the measured values to the 6S value *via* linear regression.

satellite overpass, i.e., late morning or early afternoon, yielding higher than actual daily mean values. Such overestimation was documented in many studies (**Section 1**) and recently reported by Tan et al. (2020), who compared Medium Resolution Imaging Spectrometer (MERIS) $< E_{PAR} >$ estimates against *in situ* measurements when the satellite observation was made under clear skies. In many instances, the MERIS-derived values were too high, resulting in an overall positive bias, which was explained by the presence of clouds at other times during the day.

Algorithm uncertainty was calculated for each $< E_{PAR} >$ estimate of the match-up data set, as described in **Section 3**, but is not displayed in **Figure 7**. The resulting average bias and RMSD uncertainty (includes bias and standard deviation components) are respectively 0.49 and 3.63 $Em^{-2}d^{-1}$ at BOUSSOLE, 0.70 and 4.73 $Em^{-2}d^{-1}$ at CCE-1, and 0.77 and 4.28 $Em^{-2}d^{-1}$ at CCE-2. These values resemble those obtained experimentally, i.e., 0.12 and 3.93 $Em^{-2}d^{-1}$ at BOUSSOLE, −0.49 and 3.38 $Em^{-2}d^{-1}$ at CCE-1, and 0.57 and 4.77 $Em^{-2}d^{-1}$ at CCE-2, see **Figure 7**, suggesting that the procedure to associate uncertainty is adequate and that it might not be necessary to include EPIC imagery noise in the theoretical uncertainty budget.

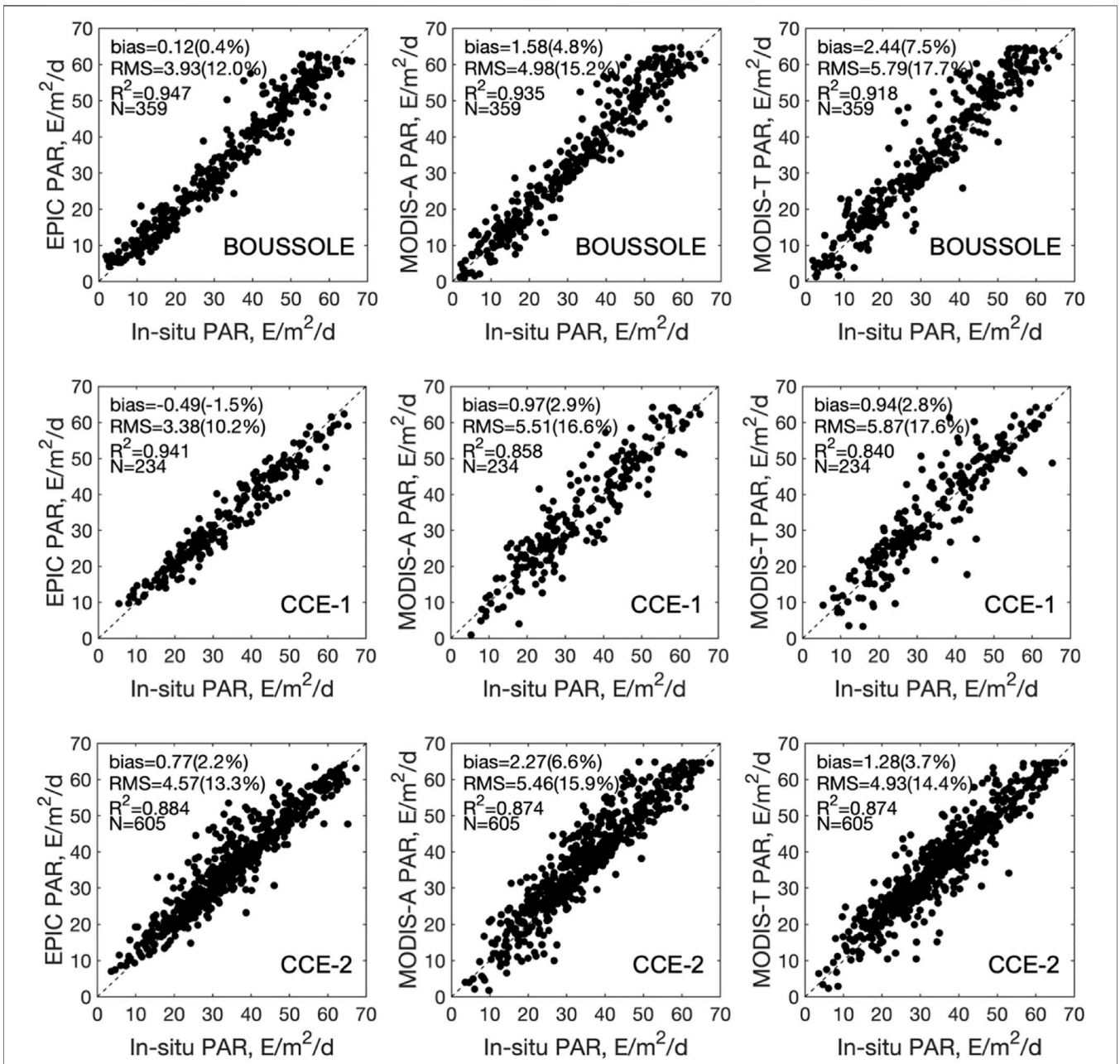

FIGURE 7 | Comparison of EPIC, MODIS-T, $<E_{PAR}>$ estimates against *in situ* data collected at the three evaluation sites (BOUSSOLE, CCE-1, and CCE-2). Left columns are for EPIC, middle columns for MODIS-A, and right columns for MODIS-T.

5 APPLICATION TO SATELLITE IMAGERY

Figures 8A–C displays an example of an EPIC $< E_{PAR} >$ product with associated uncertainties. The date is March 20, 2018 (equinox); the land is in black and the sea ice is in white. The values range from a few $Em^{-2}d^{-1}$ at high latitudes to about 58 E $m^{-2}d^{-1}$ at equatorial and tropical latitudes with atmospheric disturbances modulating the $< E_{PAR} >$ field, especially at middle latitudes (**Figure 8A**). The bias uncertainty tends to be positive when $< E_{PAR} >$ values are high (overestimation by up to 2 $Em^{-2}d^{-1}$) and slightly negative when $< E_{PAR} >$ values are low (underestimation by up to 1 $Em^{-2}d^{-1}$). The overestimation is relatively larger when $< E_{clearPAR} >$ is high and cloud factor is low, which occurs at low and middle latitudes (**Figure 8B**). The standard deviation uncertainty is more variable spatially, ranging from 2 to 8 $Em^{-2}d^{-1}$, with highest values obtained at moderate cloud factors and high $< E_{clearPAR} >$ values, as expected from **Figure 3**, for example off the coast of Chile and Peru at about 25°S and 80°W where cloud factor is about 0.5 (**Figure 8C**).

Compared with the MODIS-Aqua $< E_{PAR} >$ product (**Figure 8D**), the EPIC product (**Figure 8A**) is less noisy due to multiple observations during the day and does not have any spatial gaps at low/middle latitudes (gray color). The difference map between the two products (**Figure 9A**) shows good agreement, with higher differences generally encountered in middle to high latitude regions affected by storm activity. The MODIS-Aqua values cover a slightly larger range, which is expected because more extreme values are likely to be encountered with only one observation per day (**Figure 9B**). The frequency of values between 15 and 30 $Em^{-2}d^{-1}$ is higher for EPIC reflecting the lower probability of having very low values when several observations during the day are used in estimating $< E_{PAR} >$ in cloudy conditions. The difference histogram indicates that the EPIC $< E_{PAR} >$ values are slightly lower than the MODIS-Aqua values, by 0.7 $Em^{-2}d^{-1}$ on average (**Figure 9C**). This may result from MODIS-Aqua observing at about 1:30:pm local time, i.e., when cloudiness is usually reduced (e.g., Bergman and Salby, 1996).

The EPIC $< E_{PAR} >$ imagery of March 20, 2018, was also compared with corresponding imagery from AHI onboard Hiwamari-8 (operated by the Japanese Meteorological Agency) over the oceans and seas surrounding East and Southeast Asia and Australia (**Figure 10**). The AHI $< E_{PAR} >$ product, available at 5 km resolution on the equal latitude-longitude grid from the Japanese Aerospace Exploration Agency (JAXA) was generated from geostationary observations acquired every 10 min using an adapted version of the algorithm described in Frouin and Murakami (2007). It was remapped to the equal-angle grid (18.4 km at the equator) for comparison to the EPIC $< E_{PAR} >$ product. The spatial features are very similar in both products (**Figure 10A,B**), and differences do not exhibit a distinct pattern, although there is some evidence that larger differences often occur near the edges of low-pressure systems (**Figure 10C**). This may be due to the different temporal resolution of the two products with AHI capturing more accurately the daily variability of moving disturbances. The range of $< E_{PAR} >$ values is practically the same for EPIC and AHI, but the AHI histogram exhibits a small number of higher values between 5 and 25 $Em^{-2}d^{-1}$ and lower values above 55 $Em^{-2}d^{-1}$ (**Figure 10D**). Again, this is plausibly attributed to using more observations during the day in the AHI $< E_{PAR} >$ estimation. The $< E_{PAR} >$ differences are generally small

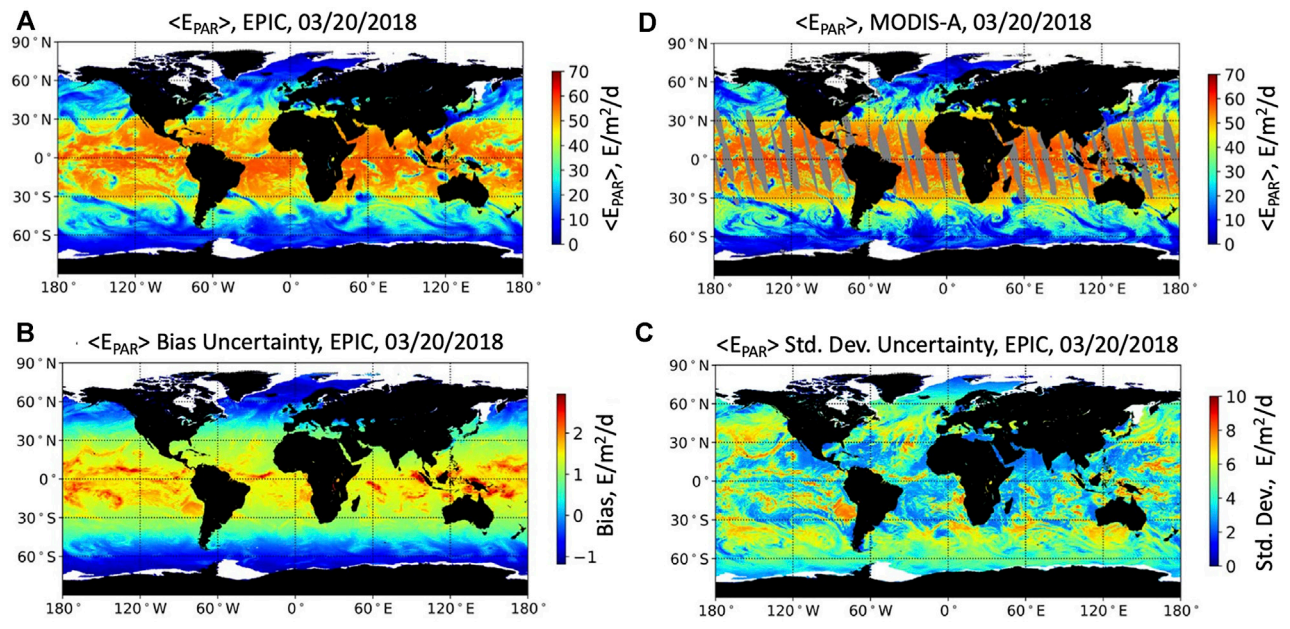

FIGURE 8 | (A) $< E_{PAR} >$ derived from EPIC imagery of March 20, 2018; **(B,C)** Algorithm uncertainty (bias, standard deviation) associated to EPIC $< E_{PAR} >$ estimates; **(D)** $< E_{PAR} >$ derived from MODIS-Aqua imagery of March 20, 2018.

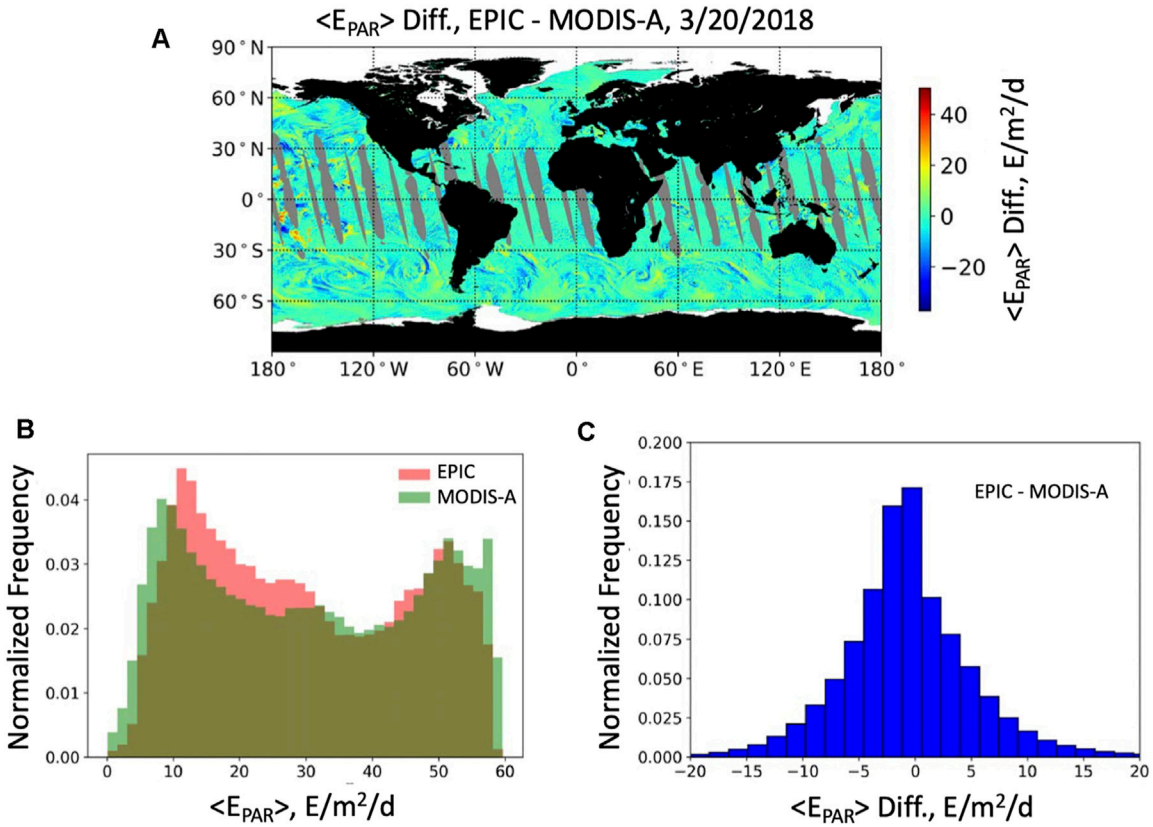

FIGURE 9 | (A) Map of the difference between EPIC and MODIS-A $<E_{PAR}>$ estimates for March, 20, 2018; **(B)** histogram of the EPIC and MODIS-A $<E_{PAR}>$ values; **(C)** histogram of the EPIC difference between EPIC and MODIS-A $<E_{PAR}>$ estimates.

(i.e., mostly between -5 and 5 $Em^{-2}d^{-1}$) but may be as large in magnitude as 20 $Em^{-2}d^{-1}$, resulting in an overall bias (higher EPIC values) of 1.34 $Em^{-2}d^{-1}$ or 3.6% (**Figure 10E**). Of course, this bias is only valid for the date and area considered in the comparison—it is expected to differ depending on region and period, yet it corresponds to a wide range of atmospheric conditions.

Figure 11 displays the time series of EPIC and MODIS daily and monthly mean E_{PAR} during the entire DSCOVR mission until August 2021 at 50°N and 30°W (North Atlantic) and 0° and 30°W (Equatorial Atlantic). The MODIS values are averages of MODIS-Aqua and -Terra estimates. The seasonal cycle and day-to-day variability are large at 50°N, while short-term variability dominates at the Equator. Seasonal E_{PAR} changes are depicted in the same way by EPIC and MODIS, but the MODIS values tend to be slightly higher, as expected. These examples of time series, and the good performance against *in situ* measurements (**Figure 7**), illustrate the potential of the EPIC $< E_{PAR} >$ product in ocean biogeochemistry studies.

6 CONCLUSION

An algorithm was developed to estimate daily mean PAR at the ice-free ocean surface, E_{PAR}, from EPIC observations in spectral bands centered on 443, 551, and 680 nm. The algorithm, based on Frouin et al. (2003), uses a budget approach that does not require distinguishing whether a pixel is clear or cloudy, which is appropriate for the coarse EPIC pixels. Algorithm uncertainties (bias and standard deviation) were associated to each $< E_{PAR} >$ estimate using LUTs established from RT simulations. A preliminary evaluation showed good agreement with $< E_{PAR} >$ estimates from other satellite sensors (polar-orbiting MODIS and geostationary AHI) and *in situ* measurements at ocean moorings. Match-up data analysis indicated that the EPIC-derived $< E_{PAR} >$ was less biased than the MODIS $< E_{PAR} >$, and the EPIC $< E_{PAR} >$ imagery was less noisy, which was explained by using multiple observations during the day with EPIC instead of only one observation with MODIS. The uncertainty of the EPIC $< E_{PAR} >$ product, with biases of −1.5 to 2.2% and RMSDs of 10.0–13.3% depending on the site is lower than the uncertainty of other parameters coming into play in primary production modeling (e.g., phytoplankton absorption and quantum yield). The $< E_{PAR} >$ 2015–2021 time series at selected oceanic locations demonstrated the algorithm ability to capture monthly to interannual variability for investigating the ocean response to temporal changes in available light over a wide range of scales.

The EPIC $< E_{PAR} >$ product is generated routinely by the NASA Center for Climate Simulation (NCCS) and distributed by

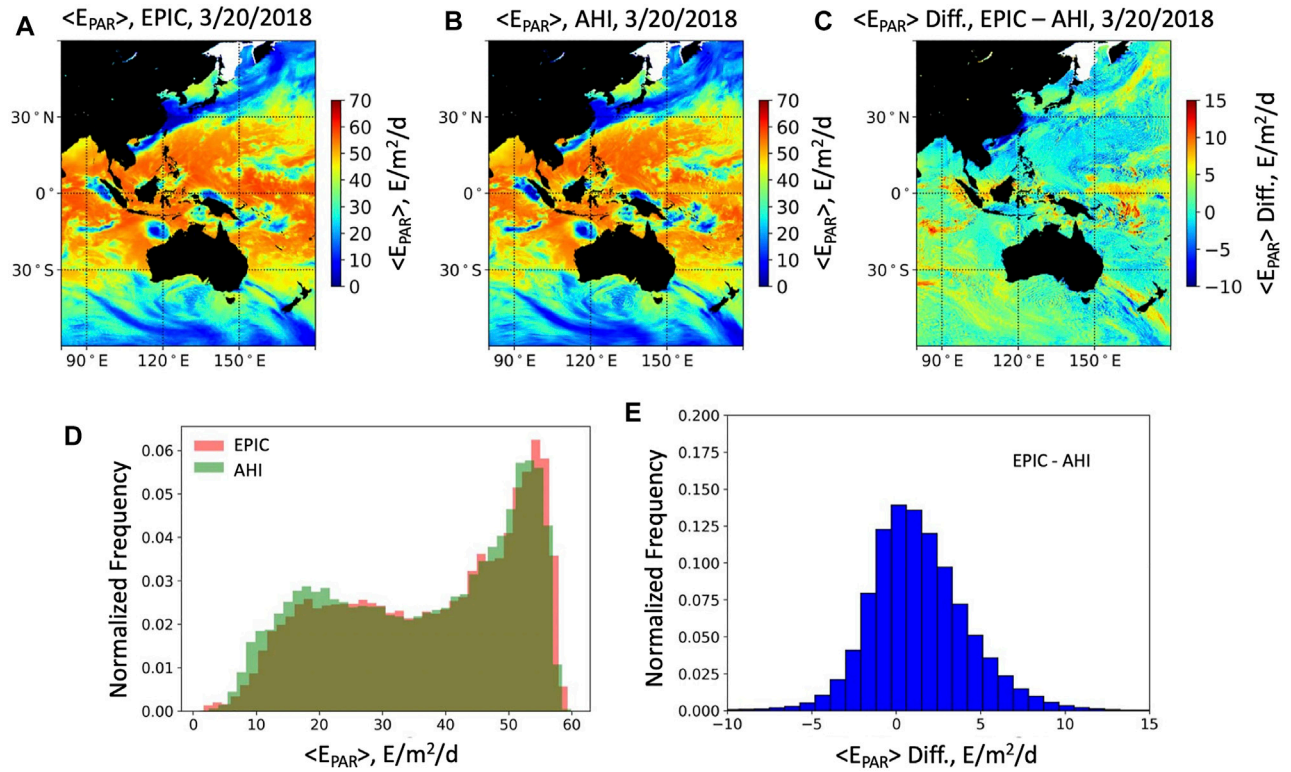

FIGURE 10 | (A) $<E_{PAR}>$ derived from EPIC imagery of March, 20, 2018; **(B)** same as **(A)**, but AHI imagery; **(C)** map of the difference between EPIC and AHI $<E_{PAR}>$ estimates; **(D)** histogram of the EPIC and AHI $<E_{PAR}>$ values; **(E)** histogram of the difference between EPIC and AHI $<E_{PAR}>$ estimates.

the Langley ASDC. The data (with documentation) are archived since the beginning of the DSCOVR mission, i.e., June 13, 2015, at https://asdc.larc.nasa.gov/project/DSCOVR/ DSCOVR_EPIC_L3_PAR_01. They are available on equidistant cylindrical Plate Carrée grid with 18.4 km resolution at the equator and in 18.4 km equal-area sinusoidal projection, i.e., on spatial grids that are compatible with MODIS and VIIRS Level 3 NASA OBPG ocean-color products.

The current algorithm can be improved in several ways, i.e., by calculating atmospheric reflectance more accurately at large zenith angles (LUTs may be used instead of approximate analytical representation), by relaxing the Lambertian assumption in the retrieval of the cloud/surface layer reflectance, by improving the parameterization of cloud bidirectional effects, and by including from reanalysis data information about cloud variability, which would provide better accuracy when only a few EPIC observations are available to estimate the daily means. Uncertainty may also be specified as a function of angular geometry and latitude, even region, instead of using an average estimate for all latitudes over several years of MERRA-2 data, and they can be fitted by a generalized additive model with proper auxiliary variables.

Other $< E_{PAR} >$ datasets exist (e.g., OBPG MODIS and VIIRS products), but the EPIC time series is uniquely valuable for several reasons. First, the daily mean PAR estimates, which exploit the multiple EPIC observations from sunrise to sunset (i.e., consider diurnal cloud variability), are more accurate than those from sensors in polar orbit (i.e., typically use one observation per day). Second, coverage is global on a daily time scale at low and middle latitudes, which is currently not achieved with instruments onboard polar orbiters (due to Sun glint, limited swath). Sensors operating from geostationary orbit have limited coverage and reduced spatial resolution at high latitudes, a smaller problem with EPIC. Third, and particularly important, comparisons between daily $< E_{PAR} >$ estimates from EPIC and concurrent polar-orbiting sensors (e.g., MODIS and VIIRS) would determine biases associated with estimates from these sensors, allowing for a consistent $< E_{PAR} >$ time series across sensors, not only during the overlap period, but before and after, i.e., for a long-term (over several decades) science quality $< E_{PAR} >$ record.

The EPIC $< E_{PAR} >$ product is useful to a wide range of research applications, such as primary production and carbon export modeling, ecosystem dynamics and mixed-layer physics, photochemical transformations of dissolved organic matter, and control of stable soluble iron in marine waters. It complements existing $< E_{PAR} >$ datasets and, as mentioned above, may bring about consistency across sensors, allowing a better description of biological phenomena that could lead to new information about temporal variability of biological processes.

The methodology can be easily extended to estimating ultraviolet (UV) surface irradiance using the EPIC spectral bands centered on 317, 325, 340, and 388 nm, especially since ozone content, a key variable governing atmospheric transmittance in the UV, is a standard EPIC product. Furthermore, planar and scalar fluxes

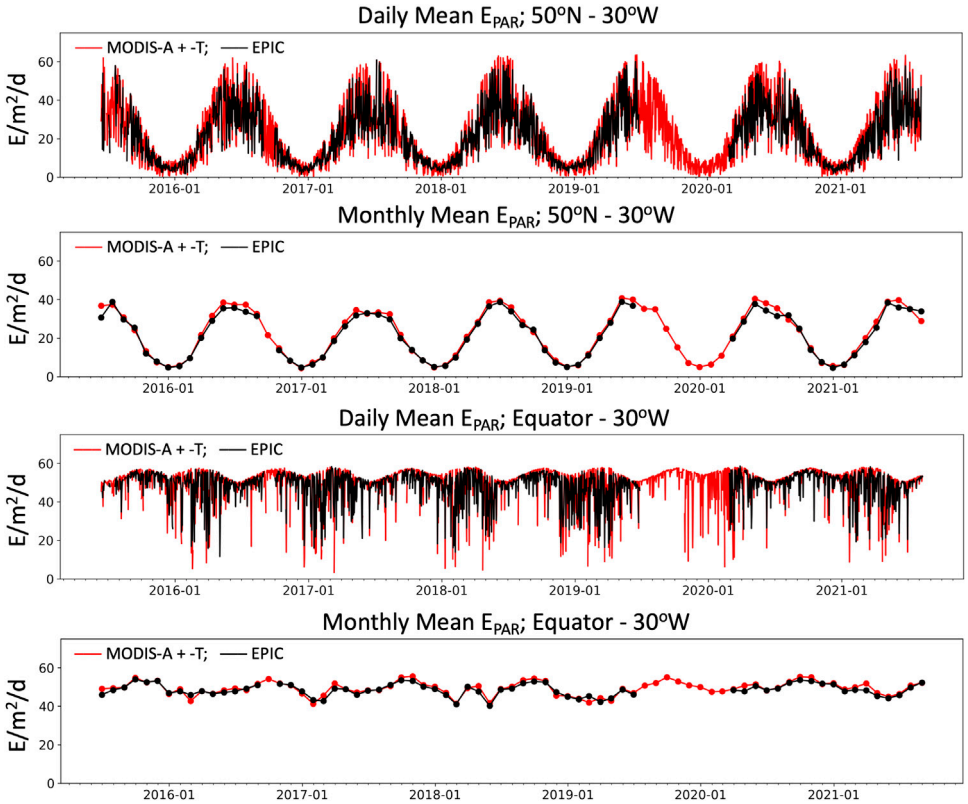

FIGURE 11 | Time series of EPIC and MODIS-A and -T daily and monthly mean E_{PAR} at 50°N and 30°W (North Atlantic) and 0° and 30°W (Equatorial Atlantic). Seasonal cycle is pronounced at 50 N and small at equator; short term variability dominates at the equator.

below the surface, as well as average cosine for total light (a measure of the angular structure of the light field), variables more directly relevant to addressing science questions pertaining to biogeochemical cycling of carbon, nutrients, and oxygen can also be estimated without major difficulty from the above-surface quantities. Approaches have been identified and procedures devised (Frouin et al., 2018a); they are based on LUTs of clear sky and overcast situations and the derived cloud factor, $< CF >$ ($< CF_{PAR} >$ for the PAR spectral range), from the EPIC observations (Frouin et al., 2018a). Following Mobley and Boss (2012), the LUTs may only depend on a reduced set of parameters, the most important ones being the location and date, which control the day length and mean Sun zenith angle, then the influence of the clouds which is between null (clear sky) and maximum (100% cloud cover), and finally the wind speed. In other words, the observed $< CF >$ may be used as a proxy for the actual cloud factor in linearly interpolating between clear sky and overcast LUTs as a function of $< CF >$. The prospects are promising for ocean biogeochemistry applications.

DATA AVAILABILITY STATEMENT

The raw data supporting the conclusion of this article will be made available by the authors, without undue reservation.

AUTHOR CONTRIBUTIONS

All the authors participated in the conception and organization of the study, the interpretation of the results, and the writing of the findings. RF and JT arranged the contents of the sections and wrote the first version of the manuscript. RF developed the algorithm to estimate ocean surface PAR. MC and DR created LUTs to associate uncertainties. JT coded the algorithms and performed the statistical analyses. MS implemented the processing line at the NASA Center for Climate Simulation and organized data archival at the Atmospheric Science Data Center. HM provided information about the AHI PAR product. DA, US, JS, and VV were involved in the field data collection and processing at the mooring sites. Everyone critically revised the manuscript.

FUNDING

The work effort to accomplish the study was funded by the National Aeronautics and Space Administration (NASA) under DSCOVR Grant 80NSSC19K0764 (Program Manager: R. S. Eckman) and by the Japan Aerospace Exploration Agency (JAXA) under GCOM-C Contract JX-PSPC-515384. The CCE moorings are funded by National Oceanic and Atmospheric Administration (NOAA) GOMO and OAP under Grant OAR4320278 Award# 304593.

The BOUSSOLE data used in this work were collected when the project was funded by the European Space Agency, the Centre National d'Etudes Spatiales (CNES) and JAXA.

ACKNOWLEDGMENTS

The authors gratefully acknowledge the various teams that produced and quality-controlled the EPIC data used in the study, the NASA OBPG for generating and making available the MODIS and VIIRS products, and JAXA for providing the AHI imagery *via* the P-Trees System. They also thank everyone involved in servicing the field instruments and collecting, processing, and archiving the BOUSSOLE, CCE-1 and CCE-2, and COVE solar irradiance data, and the MERRA-2 Science Team for the reanalysis data. The CCE-1 and CCE-2 moorings are part of the global OceanSITES program.

REFERENCES

Antoine, D., André, J.-M., and Morel, A. (1996). Oceanic Primary Production: 2. Estimation at Global Scale from Satellite (Coastal Zone Color Scanner) Chlorophyll. *Glob. Biogeochem. Cycles* 10, 57–69. doi:10.1029/95GB02832

Antoine, D., Guevel, P., Desté, J.-F., Bécu, G., Louis, F., Scott, A. J., et al. (2008). The "BOUSSOLE" Buoy-A New Transparent-To-Swell Taut Mooring Dedicated to Marine Optics: Design, Tests, and Performance at Sea. *J. Atmos. Ocean. Technol.* 25, 968–989. doi:10.1175/2007jtecho563.1

Baker, K. S., and Frouin, R. (1987). Relation between Photosynthetically Available Radiation and Total Insolation at the Ocean Surface under clear Skies1. *Limnol. Oceanogr.* 32, 1370–1377. doi:10.4319/lo.1987.32.6.1370

Ballabrera-Poy, J., Murtugudde, R., Zhang, R.-H., and Busalacchi, A. J. (2007). Coupled Ocean-Atmosphere Response to Seasonal Modulation of Ocean Color: Impact on Interannual Climate Simulations in the Tropical Pacific. *Am. Meteorol. Soc.* 20, 353–374. doi:10.1175/JCLI3958.1

Behrenfeld, M. J., Boss, E., Siegel, D. A., and Shea, D. M. (2005). Carbon-based Ocean Productivity and Phytoplankton Physiology from Space. *Glob. Biogeochem. Cycles* 19, GB1006. doi:10.1029/2004GB002299

Behrenfeld, M. J., and Falkowski, P. G. (1997). Photosynthetic Rates Derived from Satellite-Based Chlorophyll Concentration. *Limnol. Oceanogr.* 42, 1–20. doi:10.4319/lo.1997.42.1.0001

Behrenfeld, M. J., O'Malley, R. T., Siegel, D. A., McClain, C. R., Sarmiento, J. L., Feldman, G. C., et al. (2006). Climate-driven Trends in Contemporary Ocean Productivity. *Nature* 444, 752–755. doi:10.1038/nature05317

Behrenfeld, M. J., Randerson, J. T., McClain, C. R., Feldman, G. C., Los, S. O., Tucker, C. J., et al. (2001). Biospheric Primary Production during an ENSO Transition. *Science* 291, 2594–2597. doi:10.1126/science.1055071

Bergman, J. W., and Salby, M. L. (1996). Diurnal Variations of Cloud Cover and Their Relationship to Climatological Conditions. *J. Clim.* 9, 2802–2820. doi:10.1175/1520-0442(1996)009<2802:dvocca>2.0.co;2

Carr, M.-E., Friedrichs, M. A. M., Schmeltz, M., Noguchi Aita, M., Antoine, D., Arrigo, K. R., et al. (2006). A Comparison of Global Estimates of marine Primary Production from Ocean Color. *Deep Sea Res. Part Topical Stud. Oceanography* 53, 741–770. doi:10.1016/j.dsr2.2006.01.028

Cox, C., and Munk, W. (1954). Measurement of the Roughness of the Sea Surface from Photographs of the Sun's Glitter. *J. Opt. Soc. Am.* 44, 838–850. doi:10.1364/JOSA.44.000838

Curran, P. J., and Dungan, J. L. (1989). Estimation of Signal-To-Noise: a New Procedure Applied to AVIRIS Data. *IEEE Trans. Geosci. Remote Sensing* 27, 620–628. doi:10.1109/tgrs.1989.35945

Dedieu, G., Deschamps, P. Y., and Kerr, Y. H. (1987). Satellite Estimation of Solar Irradiance at the Surface of the Earth and of Surface Albedo Using a Physical Model Applied to Metcosat Data. *J. Clim. Appl. Meteorol.* 26, 79–87. doi:10.1175/1520-0450(1987)026<0079:seosia>2.0.co;2

Deschamps, P.-Y., Herman, M., and Tanré, D. (1983). *Modélisation du rayonnement réfléchi par l'atmosphère et la terre entre 0.35 and 4 μm.* France: ESA contract report 4393/8C/F/DO(SC)University of Lille, 155

Dubuisson, P., Labonnote, L.-C., Riedi, J., Compiègne, M., and Winiarek, V. (2016). "ARTDECO: Atmopsheric Radiative Transfer Data Base for Earth and Climate Observation," in Proc. International Radiation Symposium (Auckland, New Zealand, 16–22. April 2016.

Falkowski, P. G., and Raven, J. A. (1997). *Aquatic Photosynthesis*. Oxford: Blackwell.

Fitzpatrick, M. F., Brandt, R. E., and Warren, S. G. (2004). Transmission of Solar Radiation by Clouds over Snow and Ice Surfaces: A Parameterization in Terms of Optical Depth, Solar Zenith Angle, and Surface Albedo. *J. Clim.* 17, 266–275. doi:10.1175/1520-0442(2004)017<0266:tosrbc>2.0.co;2

IOCCG (2019). *Uncertainties in Ocean Colour Remote Sensing*. Editor F. Mélin (Dartmouth, Canada: IOCCG Report Series, No. 18, International Ocean Colour Coordinating Group). doi:10.25607/OBP-696

Frouin, R., and Chertock, B. (1992). A Technique for Global Monitoring of Net Solar Irradiance at the Ocean Surface. Part I: Model. *J. Appl. Meteorol.* 31, 1056–1066. doi:10.1175/1520-0450(1992)031<1056:atfgmo>2.0.co;2

Frouin, R., Franz, B. A., and Werdell, P. J. (2003). "The SeaWiFS PAR Product," in *Algorithm Updates for the Fourth SeaWiFS Data Reprocessing, NASA Tech. Memo. 2003-206892,*. Editors S. B. Hooker and E. R. Firestone (Greenbelt, Maryland: NASA Goddard Space Flight Center), Vol. 22, 46–50.

Frouin, R., and Iacobellis, S. F. (2002). Influence of Phytoplankton on the Global Radiation Budget. *J. Geophys. Res.* 107, 5–10. doi:10.1029/2001JD000562

Frouin, R., Ramon, D., Jolivet, D., and Compiègne, M. (2018b). Specifying Algorithm Uncertainties in Satellite-Derived PAR Products. *Proc. SPIE* 8525, 107780W. doi:10.1117/12.2501681

Frouin, R., and McPherson, J. (2012). Estimating Photosynthetically Available Radiation at the Ocean Surface from GOCI Data. *Ocean Sci. J.* 47, 313–321. doi:10.1007/s12601-012-0030-6

Frouin, R., McPherson, J., Ueyoshi, K., and Franz, B. A. (2012). A Time Series of Photosynthetically Available Radiation at the Ocean Surface from SeaWiFS and MODIS Data. *Remote Sensing Mar. Environ.*, 19–12. doi:10.1117/12.981264

Frouin, R., and Murakami, H. (2007). Estimating Photosynthetically Available Radiation at the Ocean Surface from ADEOS-II Global Imager Data. *J. Oceanogr.* 63, 493–503. doi:10.1007/s10872-007-0044-3

Frouin, R., and Pinker, R. T. (1995). Estimating Photosynthetically Active Radiation (PAR) at the Earth's Surface from Satellite Observations. *Remote Sensing Environ.* 51, 98–107. doi:10.1016/0034-4257(94)00068-x

Frouin, R., Ramon, D., Boss, E., Jolivet, D., Compiègne, M., Tan, J., et al. (2018a). Satellite Radiation Products for Ocean Biology and Biogeochemistry: Needs, State-Of-The-Art, Gaps, Development Priorities, and Opportunities. *Front. Mar. Sci.* 5 10778, 3. doi:10.3389/fmars.2018.00003

Gelaro, R., McCarty, W., Suárez, M. J., Todling, R., Molod, A., Takacs, L., et al. (2017). The Modern-Era Retrospective Analysis for Research and Applications, Version 2 (MERRA-2). *J. Clim.* 30, 5419–5454. doi:10.1175/jcli-d-16-0758.1

Henson, S. A., Sarmiento, J. L., Dunne, J. P., Bopp, L., Lima, I., Doney, S. C., et al. (2010). Detection of Anthropogenic Climate Change in Satellite Records of Ocean Chlorophyll and Productivity. *Biogeosciences* 7, 621–640. doi:10.5194/bg-7-621-2010

Herman, J., HuangMcPeters, L. R., McPeters, R., Ziemke, J., Cede, A., and Blank, K. (2018). Synoptic Ozone, Cloud Reflectivity, and Erythemal Irradiance from Sunrise to sunset for the Whole Earth as Viewed by the DSCOVR Spacecraft from the Earth-Sun Lagrange 1 Orbit. *Atmos. Meas. Tech.* 11, 177–194. doi:10.5194/amt-11-177-2018

JGCM-100 (2008). *Evaluation of Measurement Data—Guide to the Expression of Uncertainty in Measurement, Document Produced by Working Group 1 of the Joint Committee for Guides in Metrology (Jcgm/Wg 1), Published by the JCGM Member Organizations*, 134. Sèvres: BIPM, IEC, IFCC, ILAC, ISO, IUPAC, IUPAP and OIML.

Jin, Z., Charlock, T. P., Smith, W. L., Jr., and Rutledge, K. (2004). A Parameterization of Ocean Surface Albedo. *Geophys. Res. Lett.* 31. 1180.doi:10.1029/2004GL021180

Kahru, M., Kudela, R., Manzano-SarabiaSarabia, M., and Mitchell, B. G. (2009). Trends in Primary Production in the California Current Detected with Satellite Data. *J. Geophys. Res.* 114, C02004. doi:10.1029/2008JC004979

Kim, J., Yang, H., Choi, J.-K., Moon, J.-E., and Frouin, R. (2016). Estimating Photosynthetically Available Radiation from Geostationary Ocean Color Imager (GOCI) Data. *Korean J. Remote Sensing* 32, 253–262. doi:10.7780/kjrs.2016.32.3.5

Kirk, J. T. O. (1994). *Light and Photosynthesis in Aquatic Ecosystems*. Bristol: Cambridge University Press.

Kotchenova, S. Y., Vermote, E. F., and Frouin, E. F. (2007). Validation of a Vector Version of the 6S Radiative Transfer Code for Atmospheric Correction of Satellite Data. Part II: Homogeneous Lambertian and Anisotropic Surfaces. *Appl. Opt.* 46, 4455. doi:10.1364/ao.46.004455,

Kotchenova, S. Y., Vermote, E. F., Matarrese, R., and Klemm, Jr. (2006). Validation of a Vector Version of the 6S Radiative Transfer Code for Atmospheric Correction of Satellite Data. Part I: Path Radiance. *Appl. Opt.* 45, 6762. doi:10.1364/ao.45.006762

Laliberté, J., Bélanger, S., and Frouin, R. (2016). Evaluation of Satellite-Based Algorithms to Estimate Photosynthetically Available Radiation (PAR) Reaching the Ocean Surface at High Northern Latitudes. *Remote Sensing Environ.* 184, 199–211. doi:10.1016/j.rse.2016.06.014

Lee, Y. J., Matrai, P. A., Friedrichs, M. A. M., Saba, V. S., Antoine, D., Ardyna, M., et al. (2015). An Assessment of Phytoplankton Primary Productivity in the Arctic Ocean from Satellite Ocean Color/*In Situ* Chlorophyll- a Based Models. *J. Geophys. Res. Oceans* 120, 6508–6541. doi:10.1002/2015JC011018

Loeb, N. G., Wielicki, B. A., Su, W., Loukachine, K., Sun, W., Wong, T., et al. (2007). Multi-instrument Comparison of Top-Of-Atmosphere Reflected Solar Radiation. *Am. Meteorol. Soc.* 20, 575–591. doi:10.1175/JCLI4018.1

Longhurst, A., Sathyendranath, S., Platt, T., and Caverhill, C. (1995). An Estimate of Global Primary Production in the Ocean from Satellite Radiometer Data. *J. Plankton Res.* 17, 1245–1271. doi:10.1093/plankt/17.6.1245

Marshak, A., Herman, J., Adam, S., Karin, B., Carn, S., Cede, A., et al. (2018). Earth Observations from DSCOVR EPIC Instrument. *Bull. Amer. Meteorol. Soc.* 99, 1829–1850. doi:10.1175/BAMS-D-17-0223.1

Miller, A. J., Alexander, M. A., Boer, G. J., Chai, F., Denman, K., Erickson, D. J., et al. (2003). Potential Feedbacks between Pacific Ocean Ecosystems and Interdecadal Climate Variations. *Bull. Amer. Meteorol. Soc.* 84, 617–634. doi:10.1175/BAMS-84-5-617

Mobley, C. D., and Boss, E. S. (2012). Improved Irradiances for Use in Ocean Heating, Primary Production, and Photo-Oxidation Calculations. *Appl. Opt.* 51, 6549–6560. doi:10.1364/AO.51.006549

Murtugudde, R., Beauchamp, J., McClain, C. R., Lewis, M., and Busalacchi, A. J. (2002). Effect of Penetrative Radiation on the Upper Tropical Ocean Circulation. *J. Clim.* 15, 470486. doi:10.1175/1520-0442(2002)015<0470:eoprot>2.0.co;2

Nakamoto, S., Kumar, S. P., Oberhuber, J. M., Ishizaka, J., Muneyama, K., and Frouin, R. (2001). Response of the Equatorial Pacific to Chlorophyll Pigment in a Mixed Layer Isopycnal Ocean General Circulation Model. *Geophys. Res. Lett.* 28, 2021–2024. doi:10.1029/2000GL012494

Nakamoto, S., Kumar, S. P., Oberhuber, J. M., Muneyama, K., and Frouin, R. (2000). Chlorophyll Modulation of Sea Surface Temperature in the Arabian Sea in a Mixed-Layer Isopycnal General Circulation Model. *Geophys. Res. Lett.* 27, 747–750. doi:10.1029/1999GL002371

Platt, T., Denman, K. L., and Jassby, A. D. (1977). "Modeling the Productivity of Phytoplankton," in *The Sea: Ideas and Observations on Progress in the Study of the Seas*. Editor E. D. Goldberg (New York, NY: John Wiley, 807–856.

Platt, T., Forget, M.-H., White, G. N., Caverhill, C., Bouman, H., Devred, E., et al. (2008). Operational Estimation of Primary Production at Large Geographical Scales. *Remote Sensing Environ.* 112, 3437–3448. doi:10.1016/j.rse.2007.11.018

Povey, A. C., and Grainger, R. G. (2015). Known and Unknown Unknowns: Uncertainty Estimation in Satellite Remote Sensing. *Atmos. Meas. Tech.* 8, 4699–4718. doi:10.5194/amt-8-4699-2015

Ramon, D., Jolivet, D., Tan, J., and Frouin, R. (2016). "Estimating Photosynthetically Available Radiation at the Ocean Surface for Primary Production (3P Project): Modeling, Evaluation, and Application to Global MERIS Imagery," in *Proc. SPIE 9878" in Remote Sensing of the Oceans and Inland Waters: Techniques, Applications, and Challenges*, 98780D. doi:10.1117/12.2229892

Rossow, W. B., and Schiffer, R. A. (1999). Advances in Understanding Clouds from ISCCP. *Bull. Amer. Meteorol. Soc.* 80, 2261–2287. doi:10.1175/1520-0477(1999)080<2261:aiucfi>2.0.co;2

Ryther, J. H. (1956). Photosynthesis in the Ocean as a Function of Light Intensity1. *Limnol. Oceanogr.* 1, 61–70. doi:10.4319/lo.1956.1.1.0061

Shell, K. M., Frouin, R., Nakamoto, S., and Somerville, R. C. J. (2003). Atmospheric Response to Solar Radiation Absorbed by Phytoplankton. *J. Geophys. Res.* 108, 4445. doi:10.1029/2003JD003440

Somayajula, S. A., Devred, E., Bélanger, S., Antoine, D., Vellucci, V., and Babin, M. (2018). Evaluation of Sea-Surface Photosynthetically Available Radiation Algorithms under Various Sky Conditions and Solar Elevations. *Appl. Opt.* 57, 3088–3105. doi:10.1364/ao.57.003088

Sweeney, C., Gnanadesikan, A., Griffies, S. M., Harrison, M. J., Rosati, A. J., and Samuels, B. L. (2005). Impacts of Shortwave Penetration Depth on Large-Scale Ocean Circulation and Heat Transport. *J. Phys. Oceanogr.* 35, 1103–1119. doi:10.1175/jpo2740.1

Tan, J., and Frouin, R. (2019). Seasonal and Interannual Variability of Satellite-Derived Photosynthetically Available Radiation over the Tropical Oceans. *J. Geophys. Res. Oceans* 124, 3073–3088. doi:10.1029/2019JC014942

Tan, J., FrouinJolivet, R. D., Jolivet, D., Compiègne, M., and Ramon, D. (2020). Evaluation of the NASA OBPG MERIS Ocean Surface PAR Product in clear Sky Conditions. *Opt. Express* 28, 33157. doi:10.1364/OE.3960610.1364/oe.396066

Tan, S.-C., and Shi, G.-Y. (2012). The Relationship between Satellite-Derived Primary Production and Vertical Mixing and Atmospheric Inputs in the Yellow Sea Cold Water Mass. *Continental Shelf Res.* 48, 138–145. doi:10.1016/j.csr.2012.07.015

Tanré, D., Herman, M., Deschamps, P. Y., and De Leffe, A. (1979). Atmospheric Modeling for Space Measurements of Ground Reflectances, Including Bidirectional Properties. *Appl. Opt.* 18, 3587–3594. doi:10.1364/ao.18.003587

Uitz, J., Claustre, H., Gentili, B., and Stramski, D. (2010). Phytoplankton Class-specific Primary Production in the World's Oceans: Seasonal and Interannual Variability from Satellite Observations. *Glob. Biogeochem. Cycles* 24, a–n. doi:10.1029/2009GB003680

Wald, L. (1989). Some Examples of the Use of Structure Functions in the Analysis of Satellite Images of the Ocean. *Photogramm. Eng. Rem. Sen.* 55, 1487–1490.

Wang, Y., and Zhao, C. (2017). Can MODIS Cloud Fraction Fully Represent the Diurnal and Seasonal Variations at DOE ARM SGP and Manus Sites? *J. Geophys. Res. Atmos.* 122, 329–343. doi:10.1002/2016JD025954

Yang, Y., Zhao, C., and Fan, H. (2020). Spatiotemporal Distributions of Cloud Properties over China Based on Himawari-8 Advanced Himawari Imager Data. *Atmos. Res.* 240, 104927. doi:10.1016/j.atmosres.2020.104927

Zege, E. P., Ivanov, A. P., and Katsev, I. L. (1991). *Image Transfer through a Scattering Medium*. New York: Springer-Verlag, 349.

Zhao, C., Chen, Y., Li, J., Letu, H., Su, Y., Chen, T., et al. (2019). Fifteen-year Statistical Analysis of Cloud Characteristics over China Using Terra and Aqua Moderate Resolution Imaging Spectroradiometer Observations. *Int. J. Climatol.* 39 (5), 2612–2629. doi:10.1002/joc.5975

Conflict of Interest: Authors DR and MC are employed by HYGEOS. The remaining authors declare that the research was conducted in the absence of any commercial or financial relationships that could be construed as a potential conflict of interest.

Publisher's Note: All claims expressed in this article are solely those of the authors and do not necessarily represent those of their affiliated organizations, or those of the publisher, the editors, and the reviewers. Any product that may be evaluated in this article, or claim that may be made by its manufacturer, is not guaranteed or endorsed by the publisher.